Not all icequakes are created equal: basal icequakes suggest diverse bed deformation mechanisms at Rutford Ice Stream, West Antarctica

Sofia-Katerina Kufner (1), Alex M. Brisbourne (1), Andrew M. Smith (1), Thomas S. Hudson (2), Tavi Murray (3), Rebecca Schlegel (3), John M. Kendall (2), Sridhar Anandakrishnan (4) and Ian Lee (4)

(1) British Antarctic Survey, Natural Environment Research Council, Cambridge, UK

(2) University of Oxford, Department of Earth Sciences, Oxford, UK

(3) Swansea University, Geography, Swansea, UK

(4) Pennsylvania State University, Geosciences, and Earth and Environmental Systems Institute, University Park, PA, USA

Corresponding author: Sofia-Katerina Kufner (sofner@bas.ac.uk), ORCID 0000-0002-9687-5455

Key points

- We locate 230000 micro-earthquakes, with rupture mechanisms, at the base of a fast-flowing West Antarctic ice stream within a 3-month period
- Event distribution is little affected by tidal modulations and indicates basal sliding most affected by bed topography, stiffness and fluids
- Events occur clustered, likely due to different types of bed deformation: mobile asperities, ploughed clasts and flow-oblique bed features

Abstract

Microseismicity, induced by the sliding of a glacier over its bed, can be used to characterize frictional properties of the ice-bed interface, which are a key parameter controlling ice stream flow. We use naturally occurring seismicity to monitor spatiotemporally varying bed properties at Rutford Ice Stream, West Antarctica. We locate 230000 micro-earthquakes with local magnitudes from –2.0 to –0.3 using 90 days of recordings from a 35-station seismic network located ~40 km upstream of the grounding line. Events exclusively occur near the ice-bed interface and indicate predominantly flow-parallel stick-slip. They mostly lie within a region of interpreted stiff till and along the likely stiffer part of mega-scale glacial landforms. Within these regions, micro-earthquakes occur in spatially (<100 m radius) and temporally (mostly 1-5 days activity) restricted event-clusters (up to 4000 events), which exhibit an increase, followed by a decrease, in event magnitude with time. This may indicate event triggering once activity is initiated. Although ocean tides modulate the surface ice flow velocity, we observe little periodic variation in overall event frequency over time and conclude that water content, bed topography and stiffness are the major factors controlling microseismicity. Based on variable rupture mechanisms and spatiotemporal characteristics, we suggest the event-clusters relate to three end-member types of bed deformation: (1) continuous creation and seismogenic destruction of small-scale bed-roughness, (2) ploughed clasts and (3) flow-oblique deformation during landform-formation or along bedrock outcrops. This indicates that multiple processes, simultaneously active during glacial sliding, can accommodate stick-slip behaviour and that the bed continuously reorganizes.

Keywords

Microseismicity, icequake, basal sliding, ice stream, glacier bed, West Antarctica

1 Introduction

The potential collapse of the West Antarctic Ice Sheet remains the largest source of uncertainty in projections of future sea level rise (Feldmann & Levermann, 2015; Robel et al., 2019). This uncertainty is partly a result of incomplete ice sheet process models (Ritz et al., 2015; Tsai et al., 2015; Zoet & Iverson, 2020). Mass transfer from the ice sheet interior to the oceans is dominated by ice stream flow (Rignot et al., 2011), which, in turn, is governed by deformation within the ice, and friction and deformation at the bed, i.e. the contact between ice and underlying sediments or bedrock. Furthermore, tidally-induced modulations influence the flow dynamics of some ice streams, likely by introducing pressure modulation at the bed (Anandakrishnan et al., 2003; Gudmundsson, 2006). Poorly constrained processes and conditions at ice stream beds therefore contribute to the uncertainty in sea-level rise projections. Better understanding of the dynamic response of ice streams to a warming climate and oceans therefore requires improved models of these basal processes and the spatial variation in properties. Here we focus on the understanding of basal sliding and deformation characteristics through the analysis of naturally occurring micro-earthquakes at the ice-bed interface. These events are used to examine the nature of basal slip, tidal influences, and spatial and temporal variations.

The beds of ice streams consist of bedrock and sediment, often known as till. Till stiffness is variable and depends on the dynamic conditions and material properties. Ice flow at the bed is then facilitated by a combination of slip over a hard bed and by slip and deformation within a soft bed. Fluids further modulate basal ice stream flow. Where bedrock is exposed or subglacial till has relatively low permeability and is of low porosity, subglacial water may form a film at the ice-bed interface or accumulate in channels and pools and act to lubricate flow (Benn & Evens, 2014; Piotrowski et al., 2004). Alternatively, if the bed is composed of more permeable, high porosity till, subglacial water may penetrate, resulting in a deformable bed. Ice flow over a low permeability, low porosity bed is likely to be dominated by sliding, whereas deformation is more pronounced in the presence of more permeable, high porosity till (Blankenship et al., 1986; Reinardy et al., 2011; Stokes, 2018). In addition, drag at the glacial bed can lead to the formation of subglacial landforms, which in turn, modulate ice stream flow (Lipovsky et al., 2019; Stokes, 2018). Basal resistance may be increased at localized “sticky-spots” (Barcheck et al., 2020; U. H.

Fischer et al., 1999; Robert W Jacobel et al., 2009; Röösli et al., 2016; E. C. Smith et al., 2015), where deformation occurs through microseismicity, termed icequakes, which exhibit stick-slip behaviour. Understanding the scale and dynamics of such bed perturbations is crucial when building realistic numerical models of ice flow dynamics.

Insights into basal conditions can be gained through the study of icequakes if their hypocentres lie near the ice-bed interface (Röösli et al., 2016; E. C. Smith et al., 2015). Basal icequakes have been detected widely at glaciers in Antarctica and elsewhere (Anandakrishnan & Bentley, 1993; Blankenship et al., 1987; Danesi et al., 2007; Helmstetter et al., 2015; Röösli et al., 2016; E. C. Smith et al., 2015; Walter et al., 2008) and several reasons have been suggested for their occurrence. These include localized bed heterogeneities, water-pressure fluctuations or water-induced crack opening (U. H. Fischer et al., 1999; E. C. Smith et al., 2015; Walter et al., 2013). There is also the possibility that a combination of these mechanisms may be at play simultaneously. However, many icequake studies suffer from short deployment times or heterogeneous network geometry. This makes it difficult to isolate the effect of spatiotemporally varying basal properties on icequake occurrence. Here, we use 90 days of passive seismic data to detect basal microseismicity at Rutford Ice Stream, West Antarctica (Fig. 1). The data were recorded by 35 seismometers with a nominal spacing of 1 *km* over a 10 x 10 *km* grid deployed ~40 *km* upstream of the grounding line (Fig. 1b). Within this area, seismic surveys have shown that the bed consists of till, with varying water content, consolidation state and degree of deformation (King et al., 2016; A. M. Smith, 1997; A. M. Smith & Murray, 2009). Furthermore, it has been shown that surface ice flow is heavily modulated by a biweekly tidal signal (Gudmundsson, 2006; Minchew et al., 2017). Thus, our seismic network covers a region of diverse bed topography and rheology and captures several tidal cycles. This allows us to investigate basal slip in an ice stream with unprecedented spatiotemporal resolution. Here we locate icequakes, but also determine their source characteristics including event magnitude, source mechanisms and spatiotemporal clustering. Based on these results we can better constrain the mechanisms for seismicity and how the icequakes reveal the basal properties of the RIS.

2 Survey location

Rutford Ice Stream (RIS) (Fig. 1a) drains ~49,000 km^2 of the West Antarctic Ice Sheet into the Ronne Ice Shelf (Doake et al., 2013). To the west and east, RIS is bound by the Ellsworth Mountains and the Fletcher Promontory, respectively. At our study site, the ice flow velocity is ~375 $m\ a^{-1}$ (Adalgeirsdóttir et al., 2008) and the ice stream is around 2.2 *km* thick and grounded at 1.6-1.8 *km* below sea level (King et al., 2009). RIS occupies a deep trough with a "w-shaped" cross-section (King et al., 2016). The centre of our network is deployed on the ice stream surface above a basal central high (~1.8 *km* below sea level); the bed topography descends to the SW and NE into troughs on either site (Fig. 1b). Slightly downstream (~2 *km*) of our survey location, the bed topography is dominated by a prominent knoll, which also creates a surface expression. By contrast, the ice surface is flat within our seismic network. Nevertheless, the bed below the seismic network features a diverse morphology. This morphology can be emphasized through the 'residual elevation' (Fig. 1c), calculated by King et al. (2016) by subtracting a filtered version of the bed DEM (2 *km* x 2 *km* smoothing filter) from the original data. In the upstream part of our seismic network, the short-wavelength topography is formed of several elongated mega-scale glacial landforms (MSGLs), of which the central one is the most prominent. The topography in the downstream part of our network is more irregular and features multiple hummocks of non-uniform shape, orientation and size (King et al. (2016); Fig. 1c).

Based on radar and seismic surveys, it has been shown that the bed is composed of a basal till layer with spatially varying properties, resulting in different basal deformation regimes (King et al., 2009; Schlegel et al., 2021; A. M. Smith, 1997; A. M. Smith & Murray, 2009). Upstream, the MSGLs are likely composed of water-saturated, deformable till. Seismic surveys over these landforms, repeated over timescales of a few years, reveal sediment transport and bedform erosion of up to 1 $m\ a^{-1}$ at the downstream termination of the MSGLs (A. M. Smith et al., 2007; A. M. Smith & Murray, 2009). The deformable till layer likely overlays a stiffer and more consolidated unit that outcrops locally and predominantly northwest of the central high (Schlegel et al., 2021; A. M. Smith & Murray, 2009). Downstream of the MSGLs, the till layer is generally stiffer and likely stiffest southeast of the central high where very consolidated till or possibly sedimentary rock are proposed to exist (Schlegel et al., 2021). This first-order discrimination of

different bed domains was supported by drilling results (A. M. Smith (2020); see Fig. 1c for drill locations). In the regions of stiffer till, basal sliding rather than bed deformation predominantly accommodates basal motion at the ice-bed interface. The two domains of dominantly bed deformation and basal sliding can be discriminated from each other based on their characteristic polarity and intensity reflection values from seismic surveys (A. M. Smith, 1997). Together with the different geomorphological appearance (MSGLs vs. hummocks), this allows for the definition of a "bed character boundary" separating the two domains (King et al. (2016); G. Boulton - pers. communication in Smith et al., (2015)). This boundary is highlighted in Figures 1b/c and all subsequent map view figures. In the following, we will refer to the domain upstream of this boundary as a 'soft sediment' bed and to the domain downstream of the boundary as a 'stiff sediment' bed. This is based on the assumption that the bed character variability across the boundary mainly depends on porosity because the bed composition may be similar.

Our study site has been the focus of previous passive seismic surveys. In a pioneer study, A. M. Smith et al. (2006) deployed 10 geophones in a circular array with 3 km inter-station spacing for a 11-day observation period. The recordings from this network were not sensitive enough to allow for precise event locations but showed six times more basal micro-earthquakes originated from regions of stiff sediments. E. C. Smith et al. (2015) improved this understanding using another 10-station network, deployed in two sub-arrays with 1 *km* station spacing over a period of 35 days. Due to higher sensitivity instruments and different network configuration 3000 basal icequakes were precisely located, mostly in areas of stiff sediment bed. This confirmed findings from the earlier study and suggested that basal ice flow mechanics depend on basal conditions. Furthermore, they showed that seismicity generally featured low-angle faulting mechanisms, which indicates basal sliding in the flow direction as major source triggering seismicity.

In addition to icequake occurrence, the basal hydraulic system of RIS varies dependent on bed rheology (Murray et al., 2008). Based on radar and seismic surveys, it was shown that water channels or bodies exist in the region of soft sediments over a long distance along the landforms (at least 1 *km* long and 200 *m* wide; King et al. (2004), Murray et al. (2008) and Schlegel et al. (2021)). Furthermore, water may be present on top of MSGL ridges (King et al., 2009; Murray et

al., 2008; Schlegel et al., 2021). Within the stiffer sediment region, free water appears in isolated spots and pools (Murray et al., 2008; Schlegel et al., 2021).

Lastly, an ice stream flow velocity modulation, related to the spring-neap tidal cycle, has been measured at RIS (Adalgeirsdóttir et al., 2008; Gudmundsson, 2006; Murray et al., 2007). At the grounding line, the biweekly modulation of the surface ice stream flow velocity is up to 20%. This signal propagates, with decreasing amplitude, up to 60 *km* upstream. A linked hydrological and numerical modelling study suggests that only a combination of stress transmission through the ice and changes of basal water pressure can explain such modulations in surface ice flow velocity (Rosier et al., 2015). In addition, the model assumes a highly effective basal drainage system, low effective pressure and a nonlinear sliding law.

3 Seismic network and data processing

3.1 Network description

We use three months (mid-November 2018 to mid-February 2019) of continuous passive seismic recordings to generate a microseismic event catalogue. This dataset was collected as part of the BEAMISH project (A. M. Smith et al., 2020) during the 2018/19 field season. The seismic network broadly forms a rectangle with ~ 1 *km* station spacing. It overlays both bed-domains (Fig. 1c). The geometry of the network was modified twice during the observation period. Initially, 19 stations in the northern and central part of the network were deployed in November 2018. The network was then extended with 14 stations to the east and north in December. In January 2019, two further stations were added and three stations from the westernmost corner of the array were redeployed in the central part of the network. In total 38 sites were occupied, with 19 to 35 stations recording concurrently. During a strong storm in December, 15 of these stations were inactive for up to five days (see Fig. S1 for details).

Each station consisted of a Reftek RT-130 data logger with a 4.5 *Hz* 3-component geophone (either GS11-3D or L28-3D), which was buried to ~1 *m* depth (see Fig. S1 for details of the

network). The sampling frequency was 1000 *Hz*. Energy supply was ensured through a solar panel and battery. Timing was obtained from an attached GPS antenna.

3.2 Microseismic event catalogue and spatial clustering

Thousands of microseismic events were recorded during the deployment period. These events tend to cluster closely spaced in time, are characterized by an impulsive P-wave onset, and two prominent S-wave arrivals (Fig. 2a). The detection of two independent shear waves is an indication of the anisotropic nature of the ice comprising the RIS (E. C. Smith et al., 2017). Typical frequencies for P-waves are between 10 and 200 *Hz*. S-wave frequency is predominantly between 30 and 100 *Hz*. We use the QuakeMigrate software (Hudson et al., 2019; J. D. Smith et al., 2020) to detect and locate events from the continuous seismic records. Instead of a classic station-by-station trigger, QuakeMigrate implements a detection scheme based on the coherency of seismic phase arrivals recorded at all seismic stations. This makes it an ideal detection tool if many, temporally overlapping, small earthquakes occur. Based on the P- and S-wave onset times and uncertainties derived in QuakeMigrate, the initial locations are refined using NonLinLoc (Lomax et al., 2000), which yields a more realistic location error estimate due to a probabilistic location approach and a weighting scheme for pick uncertainties. For QuakeMigrate, we use a homogeneous velocity model (vp=3.841 $km\ s^{-1}$; vs=1.970 $km\ s^{-1}$). The P-wave velocity (vp) corresponds to the ice velocity at RIS obtained from an earlier seismic survey (A. M. Smith, 1997). The S-wave velocity (vs) is derived from vp and the vp/vs-ratio of 1.95 taken from a Wadati diagram using one day of data (~36000 P-and S-picks; Fig. S2). In NonLinLoc, we further refine the velocity model and included a uniformly 100 *m* thick layer to represent firn (vp=2.839 $km\ s^{-1}$; vs=1.456 $km\ s^{-1}$; A. M. Smith (1997)) below the seismic stations and above the solid ice. Uncertainties in the velocity model (according to A. M. Smith (1997) less than ±0.015 $km\ s^{-1}$) are assessed through relocating sample events while considering travel time dependent errors (see Section S1 for details). We do not include a velocity discontinuity below the ice, which would represent the glacial bed, as such a layer is likely to introduce artificial event-clustering (E. C. Smith et al., 2015). Theoretical calculations based on till and bed properties expected at RIS (A. M. Smith, 1997) showed that the direct upgoing P-phase likely forms the first arrival for epicentral distances of up to 10 *km*. Less than 0.01‰ of our P- and S-picks have greater epicentral distances.

Thus, including only the ice and firn layer in the velocity model does not lead to misidentified phases. Furthermore, we do not include the effect of anisotropy in ray tracing but tune QuakeMigrate through the 'detection threshold'-parameter to pick the first possible S-wave onset. We assess the effect of anisotropy by using a sample event, which is located using the first and second peak in the S-waveform, respectively (Figs. S3/S4). The discrepancy between the two resultant hypocentres is most significant in the vertical direction and can be neglected in horizontal directions, which we consider when discussing the results.

We apply quality restrictions to the automatically detected picks and events to ensure that no false picks and events are included in the final event catalogue. We accept only events with a total root-mean-square (RMS) value of travel time residual of 0.02 *s* at the maximum likelihood hypocentral location, a maximum azimuthal gap of 280°, maximum 10% of picks with a P/S travel time residual (observed subtracted by predicted arrival time) larger than 0.02 /0.2 *s*, and at least three P-picks and two S-picks. These selection criteria are obtained from the visual inspection of data sub-sets and reduce 295785 potential events initially detected from QuakeMigrate to 227029 events. Further details on location methodology and implementation to our dataset can be found in the supplementary material (S1/2 and Table S1).

We account for the movement of the seismic stations relative to the bed due to ice flow by shifting each event location in the final catalogue downstream. RIS moved ~94 *m* downstream during the 90-day survey period, whereas our stations are specified at fixed locations during event location, clearly evidencing the necessity for such a shift. We perform this shift by calculating the stations' locations at the time of each individual event relative to the start of the deployment, using their GPS locations, and apply this lateral shift to that event hypocentre. This is repeated for all events in the catalogue to compensate for ice flow.

Finally, we group the events into clusters as glacial microseismicity is known to occur in bursts of temporal and spatially focused activity (E. C. Smith et al. (2015)). We apply the DBSCAN ('Density-Based Spatial Clustering of Applications with Noise') cluster algorithms (Pedregosa et al., 2011) to search for spatial patterns in our microseismic event catalogue. This SciKit python module is designed to find core samples of high spatial density and to extend clusters around them. Only

events with magnitudes larger than the magnitude of completeness (including a 0.2 magnitude units buffer to account for uncertainty), which we determine as the maximum in the logarithmic magnitude plot of Fig. 2b, are included in the cluster analysis. This event cut-off is implemented to avoid a bias in the output clusters due to spatially differing completeness magnitudes (see details on parameterization in Section S3).

3.3 Event magnitudes

Magnitudes are calculated using a two-step approach. First, we determine the moment magnitude (M_w; Hanks & Kanamori (1979)) for a subset of our data (1st of January 2019, 1520 events) from the far-field displacement of the P-wave (Shearer (2009); implementation of Hudson et al. (2020)) and assuming density (917 $kg\ m^{-3}$) and seismic velocity (3.841 $km\ s^{-1}$) at the source (Maurel et al., 2015; A. M. Smith, 1997). We then calibrated a local magnitude scale (ML), obtained from the maximum amplitudes in the waveforms, to the M_w scale (see processing windows in Fig. 2a and processing details in supplementary material S4). We choose this two-step approach as the M_w calculation is most accurately conducted only if the focal mechanism is known and if a Brune model (Brune, 1970) can be fit to the displacement spectrum, whereas ML can be calculated for all events in our catalogue.

The derived local magnitude scale is based on Smith et al. (2015), whose local magnitude scale for RIS is adapted from the well-established but empirically derived Richter scale (Richter, 1935) and follows the equation:

$$ML = \log10(A) + m \times d_{epi} - t \qquad (1)$$

where A is the maximum amplitude of either of the two horizontal components (in instrument counts; all instruments were corrected to a consistent 'counts' scale). The distance term m accounts for the decay of amplitudes with increasing epicentral distance (d_{epi}) and t is a scaling parameter that bridges the offset between M_w and ML. We derive ML or M_w, for all stations of an event separately. The final magnitude of an event is then calculated as the median of all single-station measurements. The uncertainties are derived as the mean absolute deviation (MAD) of

the single-station ML or M_w, values from the median. Further processing steps for ML and Mw are detailed in Section S4.

We obtain a 1:1 fit (Pearson correlation coefficient of 0.96, with 1 being a linear fit and 0 being no fit) between M_w and ML for the dataset used for scaling but also a high correlation (Pearson coefficient of 0.88) when considering additional events with rupture mechanism that were not used when initially deriving the M_w-ML scaling (Fig. S5). This confirms that a linear M_w-ML scaling is adequate to fit our dataset (Butcher et al., 2020) and that the relatively simple approach of calculating ML is sufficient. This is likely because the total range of observed magnitudes spans only approximately 1.7 magnitude units (Fig. 2b) and because picks from many different azimuths are available for each event.

3.4 Event focal mechanisms and stress inversion

We determine fault plane solutions from first motion polarities and P to S amplitude ratios using the HASH software (Hardebeck & Shearer (2002), Hardebeck & Shearer (2003); implementation following Bloch et al. (2018)). As the P-wave onset of RIS microseismicity is impulsive and the signal-to-noise ratio is high (Figs. 2a, 3), an automated gradient-based polarity picker is implemented (see Section S5 for details on processing approach). Take-off angles are derived from the same velocity model used for the NonLinLoc relocations (a two-layer model of firn and ice). To account for errors in the polarity picks, 15% outliers (non-matching polarities in the final solution) are allowed during the inversion. We further perform multiple inversions while perturbing take-off angles (standard deviation of 5°) to allow for uncertainties in the velocity model and the event location. The final set of good solutions is derived based on quality criteria, which are the stability of solution upon variations of input, the azimuthal gap of the final set of stations used (should be smaller than 180°) and the final number of input picks (should be larger than seven). Due to the clear waveforms, we derive stable solutions for events in the centre of the network domain (Fig. 3a; 52% of all events with backazimuthal gap smaller than 90° have a rupture mechanism solution), but also for events at its extremities (Figs. 3b, c; 28% of all events with backazimuthal gap between 90 and 180° have a solution).

In addition to single-event solutions, we calculate cluster-wise stress tensors using all individual focal mechanisms of a cluster as input data. The stress inversion is conducted using the software slick (Michael, 1987). Slick performs a linear inversion to minimize the number of rotations around an arbitrary axis necessary to rotate the input focal mechanisms to fit a uniform stress tensor. We assess the quality of the cluster-wise solutions via bootstrap tests. In these tests, the data are resampled 100 times while the fault and auxiliary plane are exchanged for 10% of all input mechanisms. The spread of the results obtained from bootstrap inversions provides a measure of inversion robustness. We only use clusters for which more than seven mechanisms are available.

4 Results

4.1 Spatial icequake distribution and magnitudes

A map and profiles of all icequake locations are presented in Figures 4 and 5. Magnitudes range from –2.0 to –0.3 (average –1.3) with an uncertainty range of 0 to 0.4. A logarithmic plot of event number against magnitude highlights two different magnitude populations (Fig. 2b). These populations can be separated based on different decay slopes (b-values). For larger events (ML> –0.6) a b-value of 10.9 is measured. This is three times larger than the b-value of smaller events. These two magnitude populations are highlighted with different colours (small= blue; large=red) in Figures 4a and 5, aiming to convey an impression on the distribution of largest magnitude events in the study domain.

Events are generally well constrained with an average horizontal standard error (as defined by Lee & Lehr (1972)) derived from the pick uncertainties of 27 and 26 *m* in east-west and north-south, respectively. The mean vertical standard error is 48 *m*. In addition to these formal errors, we expect a perturbation of the hypocentres of ~5 *m* due to errors in the velocity model when considering the uncertainty given by A. E. Smith (1997). In addition, a more severe hypocentre perturbation arises due to seismic anisotropy. This may introduce an error of ~10-20 *m* horizontally and up to ~100 *m* vertically. Lastly, laterally variable errors in the velocity model may

329 be introduced as the firn-ice transition likely forms a gradual, rather than a sharp, velocity
330 increase (for more details on uncertainty derivation see Sections S1 and S2 and Fig. S6).

331 All events cluster near the ice-bed interface, the depth of which is derived from radar data (King
332 et al., 2016). On average, the events locate 16 *m* below the interface, which is within the average
333 vertical location uncertainty derived here and the absolute location error of 10-20 *m* given by
334 (King et al., 2016). The difference may result from velocity variations within the ice, which are
335 not captured with the two-layer model used here or from uncertainties in the absolute reference
336 frame used by King et al. (2016), or both.

337 Despite their common depth location, the events show a discontinuous spatial distribution across
338 the study region. Most events, including the largest in our dataset, locate either at the boundary
339 between the soft and stiff sediment regions or further downstream in the region of stiff
340 sediment. Within the stiff sediments, there appears to be no correlation between event density
341 and the location of hummocks identified from radar data (King et al. (2016); see geographic labels
342 in Figs. 1b and 4b for orientation). However, more events occur southwest of the central high
343 than northeast of it. In regions of very high seismic activity, events partly appear to arrange in
344 distinct regions (~ 300 – 500 *m* radius), which are seismically active at their rims and aseismic in
345 their centres (e.g., Fig. 6a). This configuration is robust, even when considering the event
346 hypocentre uncertainties. Seismicity across the transition from soft to stiffer sediments
347 correlates with a step-up in bed elevation across the boundary. If this step is large (e.g. 20 *m*
348 residual elevation increase in Fig. 5b), seismicity is most pronounced and large magnitude events
349 occur, whereas negligible seismicity is associated with a transition without a change in residual
350 bed elevation (e.g., Figs. 5a, c). Events upstream of the bed character boundary tend to occur in
351 the troughs separating MSGLs, while seismicity at the MSGL crests is absent (Figs. 5d-f).

352

353 **4.2 Event cluster characteristics and rupture mechanisms**

354 In addition to this large-scale icequake distribution, we observe a small-scale structure in the
355 spatial distribution of most icequakes. Icequakes rarely occur as single events in space and time.
356 Instead, seismicity is focused on spatially isolated spots of less than 100 *m* radius (highlighted in

Fig. 6a., zoom in of these spots in Fig. 6b), which produce many icequakes over a short timescale. We use DBSCAN to isolate these spots of focused activity, finding 828 spatial clusters with eight or more events. These clusters include 188174 events with magnitudes larger than –1.5, which means that 93% of all events with magnitudes larger –1.5 are clustered. In the following discussion, the term 'cluster' will be used to refer to discrete, spatially restricted, sites of icequake activity. By contrast, a 'temporal sub-cluster' refers to a temporally limited period of high seismic activity at the cluster location. Within temporal sub-clusters, inter-event times are in the minute range, whereas the time of quiescence between two temporal sub-clusters is on average 3.7 days (see also Section S3 and Figs. S7 & S8 for more detailed cluster characteristics).

Most clusters exhibit a common behaviour regarding their rupture mechanisms and regarding their magnitude evolution with time:

- Events within one cluster feature highly similar rupture mechanisms (example in Figs. 6b, c), resulting in well constrained cluster-averaged stress tensors (Fig. 6d). We obtain stress tensors for 428 clusters, which comprise in total 70023 individual mechanisms. The average spread value in these clusters is 4.6° (min./max.: 1.7/17.9°). The spread is a measure of how well individual mechanisms match the resulting stress tensor. This small spread value indicates highly similar focal mechanisms within each cluster.
- We observe a modulation of event magnitude within the clusters. Most ML-activity-time plots show a short-term increase and decrease of event magnitude with time (Fig. 7). On average, these activity cycles last from two to six hours (mean ~3.5 *h*) and several of these activity cycles may occur in succession (e.g. Fig. 7a). This relation is still valid when considering the uncertainty in magnitude (Fig. S9). We observe these magnitude patterns for all clusters with a magnitude range larger than ~0.4 (Fig. S10).

Despites these common characteristics, the clusters exhibit different behaviour in terms of their stress tensor-orientation relative to ice flow (Fig. 8a) and in terms of their spatiotemporal occurrence (Fig. 8b):

- We observe two dominant orientations of cluster-averaged stress tensors, which can be discriminated from each other based on their P-axes orientation. As the dip of all stress

tensors is sub-horizontal, indicating sub-horizontal sliding, the P-axes orientation can serve as a measure of the slip-direction associated to an icequake cluster. The mean P-axes azimuth of all stress inversions is 144±12°. This is comparable to the surface ice flow direction (azimuth of 148°) measured with GPS, which suggests flow-parallel sliding at the base of the ice stream. This agrees with previous source mechanism observations at RIS (Hudson et al., 2020; E. C. Smith et al., 2015). Here, the P-axes describe a gentle rotation (±11°) towards the ice stream margin on either site of the central high along with this large-scale trend. In addition, we observe a larger rotation (±36°) relative to flow for 5% (23 clusters) of all mechanisms (Fig. 8a). These mechanisms primarily occur across the bed character boundary and indicate sliding along the base but at an oblique angle relative to ice flow.

- Clusters show three distinct types of spatiotemporal behaviour. Most clusters (81%) are active only once for few days (typically <5 days) while only a smaller percentage (19%) is active multiple times for few days. These repeatedly active clusters can be grouped into either 'spatially stable' clusters (9%), which always occur at the same geographical position, albeit the ice moves above them, or in clusters where icequake hypocentres migrate downstream with ice stream flow velocity (10%; Fig. 8b). The occurrence of this different spatiotemporal behaviour is largely independent of their location with respect to the bed character boundary, the number of events in a cluster, or cluster duration (Figs. 8c/d). At the same time there is no correlation between the number of events and duration of activity (Fig. S7).

Lastly, we note that the clusters appear to range in shapes and sizes in map view (e.g. circular or elongated). However, we do not consider these variations here. Determining the exact dimension and shape of these features is at the edge of the resolution capacity of this icequake catalogue. If double-difference relocation methods were used, the single clusters might collapse to even more concentrated features.

4.3 Temporal evolution of icequake activity

Despite these pronounced spatial variations, the entire microseismic dataset shows little overall systematic temporal variation in activity, nor a strong correlation with daily or biweekly periodicities in the tidal signal at the grounding line (Fig. 9). Instead, we observe the total number of detected events and the cluster onset times to be dependent on the weather conditions at RIS (Figs. 9a-c; e). During periods of strong wind, noise levels are higher and therefore fewer events are detected. However, Figure 9 shows that approximately two months (January/February 2019) of our data were acquired during stable weather conditions and with a consistent network geometry. Although the seismic network had been active during scientific drilling in the same area (A. M. Smith et al., 2020), we do not observed a notable spatial or temporal correlation of icequakes in our catalogue and the periods of drilling (5-8th January, 18-22th January, 6-11th February; Anker et al. (2021)).

During the stable weather period, we note that a weak correlation with biweekly tidal maxima might exist when considering only events from the larger magnitude population (Fig. 9d; events with b=10.9 in Fig. 2b). For the period of stable weather conditions, the peaks in this histogram vaguely correspond to the temporal positions of the neap tides. The mean time difference of the events to the closest neap tide is 1.7 days (std of 1.0 days), whereas the mean time difference to the closest spring tide is 5.8 days (std of 1.7 days). However, apart from this weak correlation, Figure 9f illustrates the near chaotic temporal behaviour of the event clusters. For instance, the four largest clusters in our dataset behave completely differently with time. Whereas one of the clusters produces all events during ~5 days of intense activity, the other clusters are split into several temporal sub-clusters with varying numbers of events and activity times. Neither of these clusters or sub-clusters correlates with daily or biweekly trends in the tidal signal. Finally, the largest clusters (those with the highest number of individual events) do not necessarily include the events with the largest magnitude.

5 Discussion and Interpretation

5.1 Little influence of tidal forcing on icequakes

Tidally induced sea-level modulations at the grounding line have been shown to cause periodic coupling and decoupling of the ice and bed at other West Antarctic ice streams. For example, at Kamb Ice Stream (KIS), such modulations have been measured as far as 85 km upstream of the grounding line (Anandakrishnan & Alley, 1997). A likely tidally induced modulation of ice flow speed, yielding a temporally variable icequake rate has been observed at Whillans Ice Plain (WIP) (Barcheck et al., 2018, 2020; Winberry et al., 2013) as well. Also, at RIS, a biweekly modulation of ice flow velocity is observed at the surface (Adalgeirsdóttir et al., 2008; Gudmundsson, 2006; Murray et al., 2007). However, in our icequake dataset, we observe only a weak correlation between the occurrence of the largest magnitude events and the neap tide at the grounding line (Fig. 9d). This is when the glacier flow velocity at the surface reduces (Gudmundsson, 2006). A similar weak correlation of larger magnitude icequakes with the tidal cycle has been observed before (Adalgeirsdóttir et al., 2008; E. C. Smith et al., 2015). Although this trend is weak, it has been observed in three different datasets, collected in different years (1997-1998, 2008-2009 and 2018-2019), so is likely a characteristic of basal microseismicity at RIS. Although magnitude variation can be caused by a number of other factors (e.g., fault size, variable loading velocity), a temporal modulation of icequake magnitudes could suggest that the pressure regime at the ice-bed interface changes temporally. The two different b-value trends we observe for our dataset (Fig. 2b) also allude to this. Variable b-values can occur due to changes in the stress regime during the observation period (El-Isa & Eaton, 2014) or during the transition from tectonic to fluid assisted failure (Kettlety et al., 2019).

However, apart from the possibility of a gentle magnitude modulation with the tidal cycle, the bulk of basal seismicity does not show any clear biweekly trend. A correlation between icequake intensity and daily tidal height at the grounding line is not observed either. Thus, our observations contrast with the results at KIS or WIP, where variations of seismicity rates with one or two daily peaks, often but not always associated to the tidal cycle, have been observed (Anandakrishnan & Alley, 1997; Pratt et al., 2014). At KIS basal icequakes are thought to accommodate significant

parts of the basal ice stream motion (Anandakrishnan & Alley, 1997). At WIP, microseismic events likely indicate the nucleation phase for a tidally induced large-scale movement of the ice stream (Winberry et al., 2013). Furthermore, Barcheck et al. (2020) inferred an alignment of seismicity and MSGLs. This basal seismicity is periodic and influenced by glacial flow variations, likely produced by the tidal cycle.

The situation at RIS is clearly different and prompts two possible interpretations. On one hand, our observations could be explained by a scenario where basal sliding varies temporally, like the observed surface modulation, but is not reflected by stick-slip seismicity at the bed. Thus, icequakes would make up only a small proportion of the total motion and the tidal signal could be accommodated by aseismic deformation and movement at the bed (E. C. Smith et al., 2015). On the other hand, there could be intra-ice deformation at RIS, which modulates the deformation signal from the surface to the bed. Such tidally-induced modulations in the vertical strain rate have recently been detected in ice sheets (Vankova & Nicholls, 2019). Furthermore, the ice at RIS is much thicker than at WIP (2200 *m* at RIS, 650-800 *m* at WIP; Fretwell et al. (2013)), which could explain why intra-ice deformation has a larger impact at RIS. In addition, at RIS, icequakes along the MSGLs occur with a similar spatial distribution to WIP but without a clear temporal pattern. This discrepancy would be an argument for tidal forcing at the base of RIS being less pronounced than at other ice streams. In addition, the bed topography of RIS is more extreme (see e.g. Fig. 1c), compared to the relatively flat bed of WIP, which might hinder the upstream propagation of a tidally induced pressure change along the ice-bed interface. On the contrary, in modelling studies, tidal forcing has been suggested to periodically modulate the surface ice flow via friction at the bed (Rosier et al., 2015). This would require the tidal signal at the bed to be even more pronounced than at the surface and would be an argument for dominantly aseismic motion at the bed of RIS. Ultimately, measurements that monitor the strain or fabric modulations through the ice column might help to discriminated between these different scenarios. However, in either case, this study shows that the basal seismicity at RIS is not, to first order, controlled by the tidal cycle.

5.2 Network wide icequake distribution: Role of bed topography, bed properties and water in triggering icequakes

As the tidal influence in icequake distribution appears minor, other characteristics, such as bed topography and till properties at the bed, must have a greater impact on temporal and spatial icequake distribution. Soft till will accommodate ice flow by deformation whereas stiff till favours basal sliding (A. M. Smith, 1997). Accordingly, and in agreement with previous icequake studies at RIS (A. M. Smith, 2006; E. C. Smith et al., 2015), we observe more icequakes within the stiffer bed domain than in the soft sediment units (see Maps in Figs. 1c and 4b for the geographic locations used in the following discussion). However, due to the superior network configuration and size compared to previous studies, we observe previously unresolved second order structures. We observe, for instance, fewer icequakes northeast of the central high than southwest of it within the broad domain of stiff sediments downstream of the bed character boundary. A lower radar reflectivity has been inferred for the latter, which suggests outcropping bedrock or very compressed sediments (Schlegel et al., 2021). Thus, larger regions of reduced seismicity within stiff till units could indicate the presence of compressed sediment or outcropping bedrock.

Furthermore, the icequake distribution highlights features that we suggest indicate variations in bed character over scales of hundreds of meters. This can best be illustrated within the soft sediment upstream of the bed character boundary, where we observe large-scale flow-parallel alignment of events within the valleys separating MSGLs (e.g., Fig. 5d). This suggests that stiff till must be present in the valleys to favour seismogenic stick-slip behaviour. Barcheck et al. (2020) inferred similar alignment of seismicity and MSGLs at WIP. They also related these patterns to changes in frictional properties (soft sediments on top, stiffer at base). This alignment could be due to either the constructional or erosive creation of MSGLs. In both cases, soft sediments would be expected at the MSGLs crests. However, at RIS, seismic studies showed that MSGLs likely form when soft deformable sediments are accumulated (A. M. Smith et al., 2007). Thus, the similar character of seismicity at WIP and RIS might hint toward a constructional creation of MSGLs in general.

Another bed feature at the scale of a few hundreds of meters highlighted by our icequake catalogue is the seismicity arranged in circular patterns with the centres depleted in seismicity within the broad domain of stiff sediments (e.g., Fig. 6a). At least one of these central regions corresponds to an area where free water is proposed to exist at the glacier bed (Schlegel et al., 2021). However, we can rule out a direct role of fluid in creating icequakes through tensile crack opening as the RIS icequakes are likely caused by a double-couple source. Icequakes directly triggered through the hydraulic system at the glacial bed may manifest themselves through non-double-couple tensile crack faulting (Walter et al., 2013). We infer the double-couple nature of the RIS icequakes from the station coverage that allows for many rupture mechanisms the coverage of the entire focal sphere (e.g., Fig. 3a). If the icequake source would have a significant non-double-couple component, a less clear separation of positive and negative polarities close to the nodal planes would be expected. In addition, results of full-waveform modelling for one icequake at RIS show a double-couple source to be more likely (Hudson et al., 2020). Full-waveform modelling would allow for the resolution of different source types. Thus, both studies suggest that neither the direct role of fluids (e.g., through hydrofracturing) or other processes that require tensile forces (e.g., crevasse opening) seem to drive the icequakes at RIS. Instead, we propose that a weakening of the till resulting from the presence of fluid penetrating the till layer (Rathbun et al., 2008) or fluctuations in the hydraulic pressure caused by fluids (Röösli et al., 2016) may eventually result in a series of stick-slip events adjacent to regions of free water at the ice-bed interface. The role of fluids in promoting icequakes would also explain the temporal and spatial event clustering we observe (T. Fischer et al., 2014; Greenfield et al., 2019) and the large b-values (El-Isa & Eaton, 2014; Schlaphorst et al., 2017; Wilks et al., 2017). Large b-values are indicative for swarm-like earthquake behaviour, which, in turn can be triggered from fluid induced pressure variations.

5.3 Zooming into individual icequake clusters: Types of subglacial stick-slip deformation

Icequakes typically occur clustered in space and time, as observed at the bed of other glaciers in Antarctica and elsewhere (e.g., Danesi et al. (2007); Helmstetter et al., (2015); Barcheck et al.,

(2020)). Despite cluster nature, size and repeat time being highly variable, clustered icequake activity is generally interpreted to be caused by sticky-spots (Barcheck et al., 2020; U. H. Fischer et al., 1999; Robert W Jacobel et al., 2009; Röösli et al., 2016; E. C. Smith et al., 2015), where basal resistance increases. Although descriptive, this interpretation does not necessarily imply a specific physical mechanism. Also, at RIS, we observe a large spatiotemporal variability of cluster nature. Due to the relatively long observation period and large network aperture compared to previous studies, as well as the detailed knowledge of bed properties from seismics, drilling and radar, we suggest that sticky-spots at RIS can be attributed to three different end-member types of stick-slip behaviour at the glacier bed, which are schematically shown in Figure 10. We note, however, that there is likely no strict separation between these different end-member types and they can occur simultaneously or intermingled. As a whole they may be indicative of the deformation characteristics of subglacial till beds.

In the following interpretation it is assumed that all icequakes occur very close to the ice-bed interface. This assumption is justified as the vertical location uncertainty (Fig. S6), including possible effects of model errors and anisotropy (Sections S1 and S2), and the uncertainty in the radar-constrained interface (King et al., 2016), places all events at the interface. This agrees with full-waveform source inversions that suggest that such icequakes at RIS occur within metres of the ice-bed interface (Hudson et al., 2020). Furthermore, we note that our event catalogue does not allow us to draw detailed conclusions on the shape of the individual clusters. The event cluster size is generally in the 10 to 100 *m* range and with variable shape. However, based on the location errors derived from the pick uncertainties and additional uncertainty from unmodelled errors in the velocity model (isotropic and due to anisotropy), it is likely that the different shapes of individual clusters may be within the location uncertainty. Thus, all events in one temporal sub-cluster may originate from a single spatial location, i.e., a single fault.

5.3.1 Type 1 - Self-destructive asperities: Most of the icequake clusters (81%) are active for less than five days (mean 3.5 days, std 8.4 days; Figs. 8d/S7a). During this time, the ice stream flows ~3.7 *m* downstream. We detect icequakes with inter-event times in the one- to five-minute range (mean 4.6 minutes, std 9.3 minutes; Fig. S7d). These clusters are then inactive for the remainder

of our observation period, which suggests that these spots are unlikely to be stationary obstacles in the ice stream bed. Stationary obstacles would likely produce repeating seismicity, e.g., upon variations in basal water pressure (U. H. Fischer et al., 1999) or due to constant ice loading. Instead, we favour a concept of asperities within the subglacial till, which are randomly built by the glacial movement and subsequently destroyed through a sequence of stick-slip events. Such asperities may be envisaged as sites of increased friction that develop during continuous ice stream movement as sediment is transported and dilates and reorganizes (McBrearty et al., 2020; Thornsteinsson & Raymond, 2000; Van Der Meer et al., 2003). If glacial till is sheared, its pore volume is increased (Boulton & Hindmarsh, 1987). Till can then be weakened if pathways that permit water flow into the dilated material exist (Rathbun et al., 2008). This may lead to the formation of an asperity along which slip-deficit can build-up. Freezing-on of part of the bed could additionally contribute and would favour velocity weakening (Lipovsky et al., 2019), which is a requirement for stick-slip behaviour. Once the shear resistance of the asperity is overcome, stress is released in a series of icequakes and the specific asperity is destroyed. The displacement per event at RIS is estimated to be in the range of 0.03 to 0.07 *mm* (E. C. Smith et al., 2015), which is less than the glacial movement that would accumulate during typical inter-event times (~0.8 *mm* min^{-1}, assuming the same velocity at the base of the ice stream and the surface). Thus, it is unlikely that each new event in an icequake cluster is created by continuous loading. It rather suggests that a spot mostly deforms aseismically but slip-deficit can accumulate occasionally. As we rarely observe single events, but event clusters, it appears that glacial till does not support the accumulated slip-deficit to be released in a single large event (e.g. comparable to megathrust earthquakes in subduction zones), but rather in many small icequakes. If the asperities develop due to the ice stream movement and reorganization of till, different event counts per clusters, as observed here, can be envisaged. The sharp magnitude cut-off at larger magnitudes (b-value of 10.9) obtained here might also suggest that an upper magnitude threshold exists for the largest possible icequake. This magnitude threshold may be governed by the till properties and the maximum available normal stress.

In this concept of self-destructive asperities, the bed material must be strong enough to allow for the build-up of stress locally. This may explain why more icequakes clusters occur in the stiff-sediment domain. Furthermore, the bed character boundary sections with a large step in residual topography may be favoured for the occurrence of such clusters as they represent natural obstacles for flow. On the contrary, it seems that very stiff surfaces, like the stiff-sediment units northeast of the central high, are less favourable for asperity formation. This may be as sediment reorganization is expected to happen more slowly. Instead, they may give rise to polished surfaces, possibly overlain by a homogeneous water film, where aseismic glacial sliding is the dominant basal motion process.

5.3.2 Type 2 - Ploughed clasts: For some clusters (numbering 72 – 9% of all clusters), we observe the downstream migration of the seismically active sites at the same speed as ice flow at the surface, which is ~1.05 $m\ day^{-1}$ (Fig. 8b). This phenomenon occurs for ~50% of all clusters which are active for a sufficient duration that the observed migration is larger than the single event location uncertainty. This observation suggests that an object, held within the ice, is being transported downstream and causing the icequakes. During this transportation process the spot is periodically seismically active. Likely candidates for such a mobile object are clasts held in the basal ice and dragged through the glacial sediments or over harder materials (Zoet & Iverson, 2020). The presence of clasts embedded in the bed had been proposed based on scientific drilling at RIS (A. M. Smith et al., 2020). If clast motion is hindered for some time, allowing slip-deficit to accumulate, the seismic activity could represent the moment in which the clast slips forward. An icequake with double-couple source would then be created by frictional sliding between the clast and/or the ice and till layer. Laboratory experiments showed that ploughing clasts can cause velocity weakening behaviour (Iverson, 2011; Thomason & Iverson, 2008). The clast may eventually become lodged due to melt out or changes in the properties of the sediment. Such clasts will have variable shape, size and penetration depth, and so different numbers of events in the clusters appears logical. Our event catalogue does not allow us to comment on the size or shape of such clasts, as we consider them to be within the horizontal resolution of the event locations. In contrast to icequakes originating from breaking asperities, bed deformation is expected in the case of ploughed clasts (Zoet & Iverson, 2020).

Apart from downstream migrating clusters, we observe some clusters (numbering 82 – 10% of all clusters) that are active repeatedly at the same location (Fig. 8b). These could represent the presence of a more permanent obstacle to ice flow. Either basal drag could be too weak or the till matrix too strong to allow for the mobilization of a clast. Alternatively, these clusters could be related to bed asperities. Part of an asperity may remain locked after the initial cascade of icequakes and break at a later stage.

5.3.3 Type 3 – Flow-oblique landforms as obstacles: Our stress inversion dataset contains 23 clusters (5% of all clusters with stress inversion results) that indicate flow-oblique deformation (Fig. 8a). This rotation (±36°) is clearly supported by the data. For instance, seismic stations, crucial for constraining the rupture mechanism, show different polarities for either flow-parallel or flow-oblique mechanisms (Figs. 3b, c). Furthermore, the rotated events occur close to mechanisms that are not rotated. Thus, their occurrence is unlikely to be an effect of network geometry. Such flow-oblique mechanisms have not been observed at RIS before and we suspect that it is the dense seismic network and the low noise level that allows them to be resolved here. Based on our first-motion mechanisms we infer that the main difference between these icequakes and those discussed above is the rotation of the strike of the rupture mechanism. A comparative analysis of the source characteristics of the different icequake populations might yield further discrimination.

Although scenarios can be envisaged where rotated rupture mechanisms originate from self-destructive asperities of ploughed clasts, it is striking that these mechanisms mainly occur along the bed-character boundary and at the termination points of MSGLs. This suggests a causal relationship. These flow-oblique focal mechanisms may be related to intra-till deformation that occurs during the formation of subglacial landforms – either at the ice-bed interface or within the deforming till. This agrees with laboratory experiments conducted by Lipovsky et al. (2019), who concluded that shear seismicity may indicate geomorphological activity. Here, the flow-oblique mechanisms occur mostly along the bed character boundary. The bed character boundary is thought to be modified over time scales of a few years by sediment deformation

667 (King et al., 2016; A. M. Smith & Murray, 2009). Furthermore, the flow-oblique mechanisms tend
668 to focus along the termination points of MSGLs, where active erosion and deposition has been
669 interpreted from seismic data (A. M. Smith et al., 2007). A. M. Smith et al. (2007) concluded that
670 sedimentary processes may be the most likely explanation for this erosion. The flow-oblique focal
671 mechanisms are likely the brittle manifestation of such sedimentary processes. Alternatively, or
672 in addition, the flow-oblique focal mechanisms may originate at outcropping bedrock. Such
673 bedrock units cannot be eroded and may form an obstacle that creates a local distortion of the
674 stress regime.

675

676 **6 Summary and outlook**

677 We present a microseismic event catalogue for a 10 x 10 *km* region, ~40 *km* upstream of the
678 grounding line of RIS. The seismic network used to derive this catalogue straddles a change in
679 bed character properties (soft to stiff sediments) with consistent station spacing. Thus, we can
680 identify seismic and aseismic regions within our network domain with high certainty.

681 All ~230000 micro-earthquakes (magnitudes between –2.0 and –0.3) detected in a 90-day
682 observation period are located near the ice-bed interface. Most of these events indicate flow-
683 parallel stick-slip. We propose that the interplay between the topography, bed character type
684 and the hydraulic system at the bed controls the spatiotemporal patterns in icequake occurrence.
685 Icequakes focus at the transition from soft to stiff till and in defined spatial domains of stiffer till.
686 The domains within stiffer till can be either large, coherent regions or more subtle structures, like
687 the valleys separating MSGLs. Within the regions of stiffer till, fluids may modulate the strength
688 of the till to promote seismicity. In contrast, tidally induced pressure fluctuations at the bed seem
689 to be less pronounced or have little effect on icequake occurrence. This suggests that part of the
690 tidally induced modulation is taken up by aseismic bed or intra-ice deformation.

691 On a smaller scale, most icequakes (93%) occur in clusters that are spatially and temporally
692 restricted bursts of seismic activity. Accordingly we measure high b-values (between 3.3 and
693 10.9) in event number-magnitude plots, which are indicative for swarm-like behaviour of
694 earthquakes (El-Isa & Eaton, 2014). Modulations in b-values might be due to pressure

fluctuations at the ice-bed interface or indicate an upper limit for the maximum icequake size. These clusters are generally less than ~100 *m* in radius and are active for only a few days. Based on the calculated location uncertainty, we suspect that all events in a specific cluster could originate from the same spatial spot, i.e. a single fault. These clusters show an increase and decrease of event magnitude with time while the events in a specific cluster feature highly similar rupture mechanisms. We further observe a gentle correlation of increasing inter-event times with increasing magnitudes. Similar icequake characteristics have been observed in very different glacial settings in the European Alps and in Greenland (Helmstetter et al., 2015, 2018; Röösli et al., 2016), although observation time spans in these studies are shorter than in this study. Thus, these common characteristics may provide insight to the rupture mechanism of icequakes, i.e. the rupture of an asperity surrounded by aseismic slip, in general. Furthermore, such common characteristics hint towards a unique driving force within a cluster and suggests event triggering within the clusters once the activity period is initiated, possibly facilitated by frictional heating. A detailed investigation of the source mechanisms, the inter-event locations (e.g., through double-difference methods) and of the material properties surrounding the events might help to discriminate between such processes.

Apart from these common features, the clusters can be discriminated from each other based on distinct spatiotemporal evolution characteristics and the orientation of rupture mechanisms relative to ice flow. We attribute their distinct characteristics to different end-member deformation mechanisms that may act at the bed simultaneously. These are the dynamic creation and seismogenic destruction of spots of increased friction that develop due to sediment transport and/or due to temporal variable till properties (‘asperities’), the ploughing of clasts through the underlying sediment, and flow-oblique deformation either associated with the erosion and formation of subglacial landforms or due to bedrock obstacles at the ice stream bed. Among these, the seismogenic destruction of asperities is the most common process. Taking these different processes together, we conclude that the bed of RIS can be envisaged as an actively and heterogeneously deforming subglacial bed mosaic (Piotrowski et al., 2004) with a variety of deformation processes active simultaneously. Our analysis suggests that the friction at

the bed varies over a small scale and that the glacial bed is in a process of continuous reorganization. Both impact ice stream flow directly.

Acknowledgements

This work was funded by NERC AFI award numbers NE/G014159/1 and NE/G013187/1. We thank the staff at Rothera Research Station and BAS logistics for enabling the fieldwork associated to this project and the BEAMISH field team (2018/19) for acquiring the passive seismic data. Seismic instruments were provided by NERC SEIS-UK (Loan 1017), by BAS and by the Incorporated Research Institutions for Seismology (IRIS) through the PASSCAL Instrument Center at New Mexico Tech. The facilities of the IRIS Consortium are supported by the National Science Foundation's Seismological Facilities for the Advancement of Geoscience (SAGE) Award under Cooperative Support Agreement EAR-1851048. Jamie Oliver (BAS) helped in preparing the schematic sketch of Figure 10. We thank three anonymous referees for useful comments that improved the manuscript.

Data Availability

The data, which supported the main findings of this work (icequake catalogue, rupture mechanisms and seismic station meta data), are available via the UK Polar Data Centre: https://doi.org/10.5285/B809A040-8305-4BC5-BAFF-76AA2B823734 (Kufner et al., 2020). Raw seismic data is registered under the FDSN network code 9B (2016-2019; https://doi.org/10.7914/SN/9B_2016).

Figures:

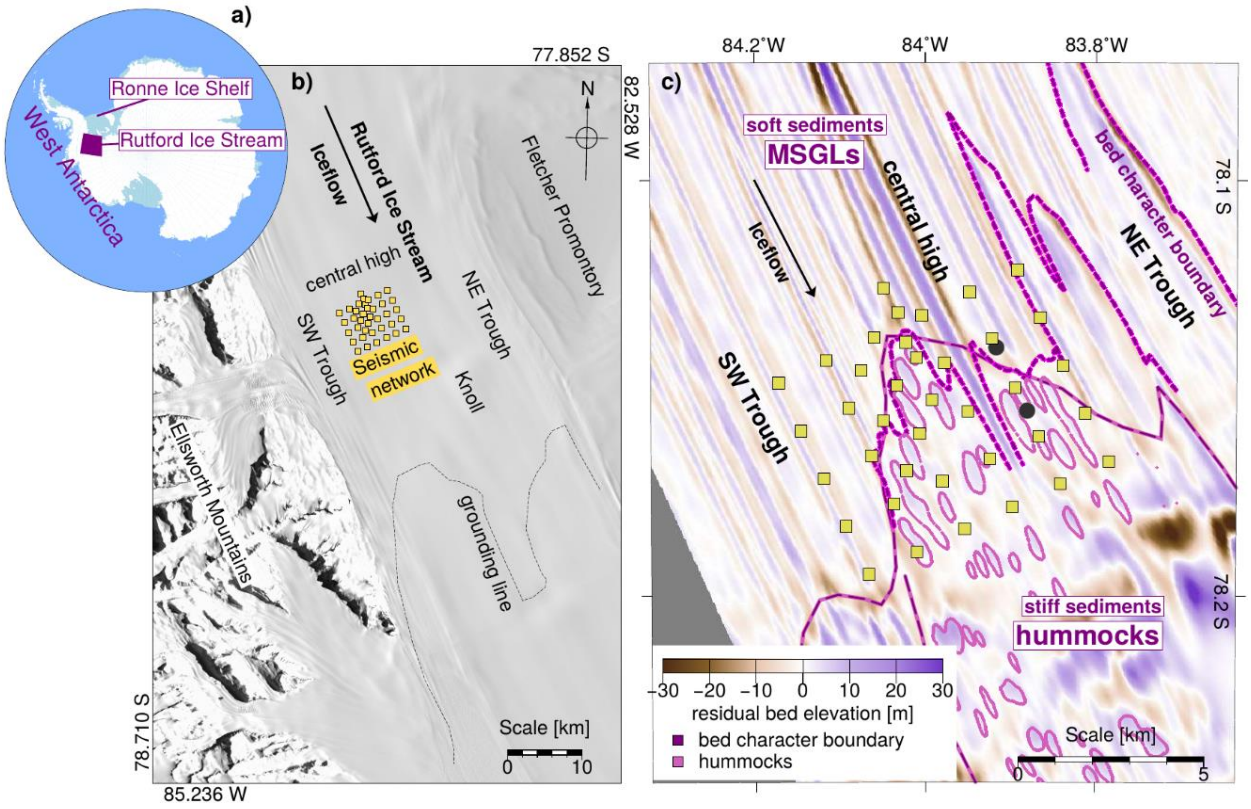

Figure 1: Study location. a) Location of Rutford Ice Stream (RIS). b) Location of seismic deployment at RIS, stations shown as yellow squares. Background shows the LIMA (Landsat Image Mosaic of Antarctica) image (USGS, 2007) of RIS. A plan view of the stations with their identifiers, deployment times and instrument types is included as Figure S1. c) Zoom into the study region. Background colour coding demarcates residual bed topography, which is calculated based on the difference between the short-wavelength topography and a long-wavelength trend surface (King et al., 2016). Hummock locations and dashed bed character boundary are from King et al. (2016), while the dotted pink-purple line represents an alternative bed character boundary defined by G. Boulton (pers. communication in Smith et al. (2015)). Gray circles indicate the location of hot-water drill sites that where operated during the BEAMISH 2018/19 season (A. M. Smith et al., 2020).

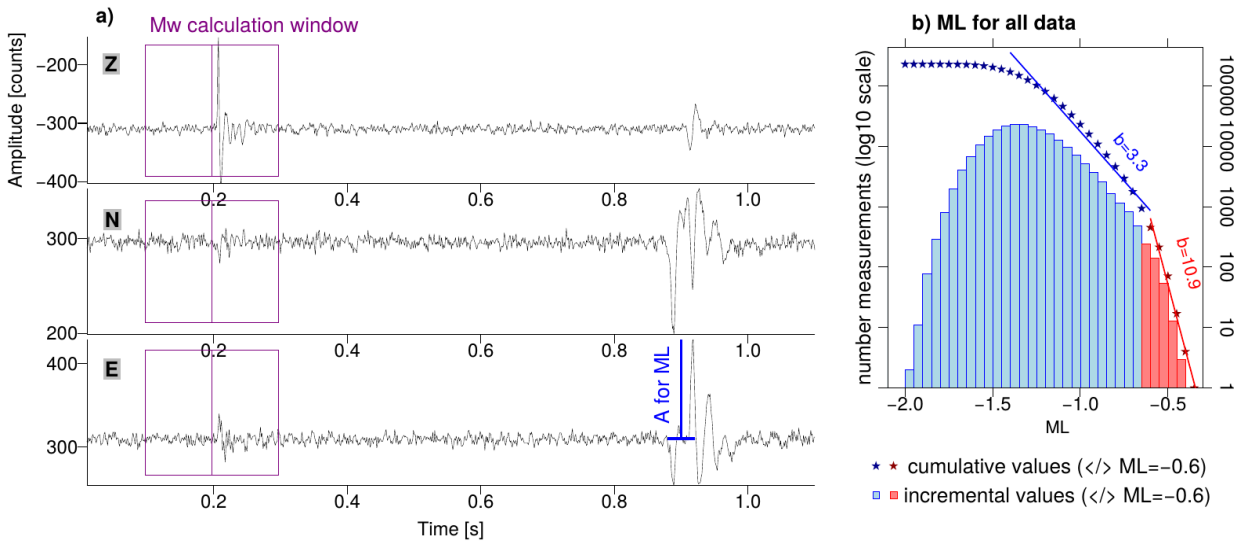

Figure 2: Data example and magnitude histogram. a) Three components (Z- vertical; N/E - horizontal towards North/East) of a magnitude –0.9 icequake (event time: 2019-01-27T02:58:13.874) recorded at station R2040 (map of the station identifiers is given as Figure S1). Amplitude is in instrument counts. The windows used for M_w derivation and the maximum amplitude used to calculate ML are highlighted. b) Magnitude histogram for all events in 0.05 bins. 'Cumulative values' refer to the all events greater or equal to a specific magnitude according to the Gutenberg-Richter law (Gutenberg & Richter, 1944). Solid lines represent regression lines based on the cumulative values. Sections with different log(ML) decay slopes ('b-values') are highlighted in red and blue, respectively.

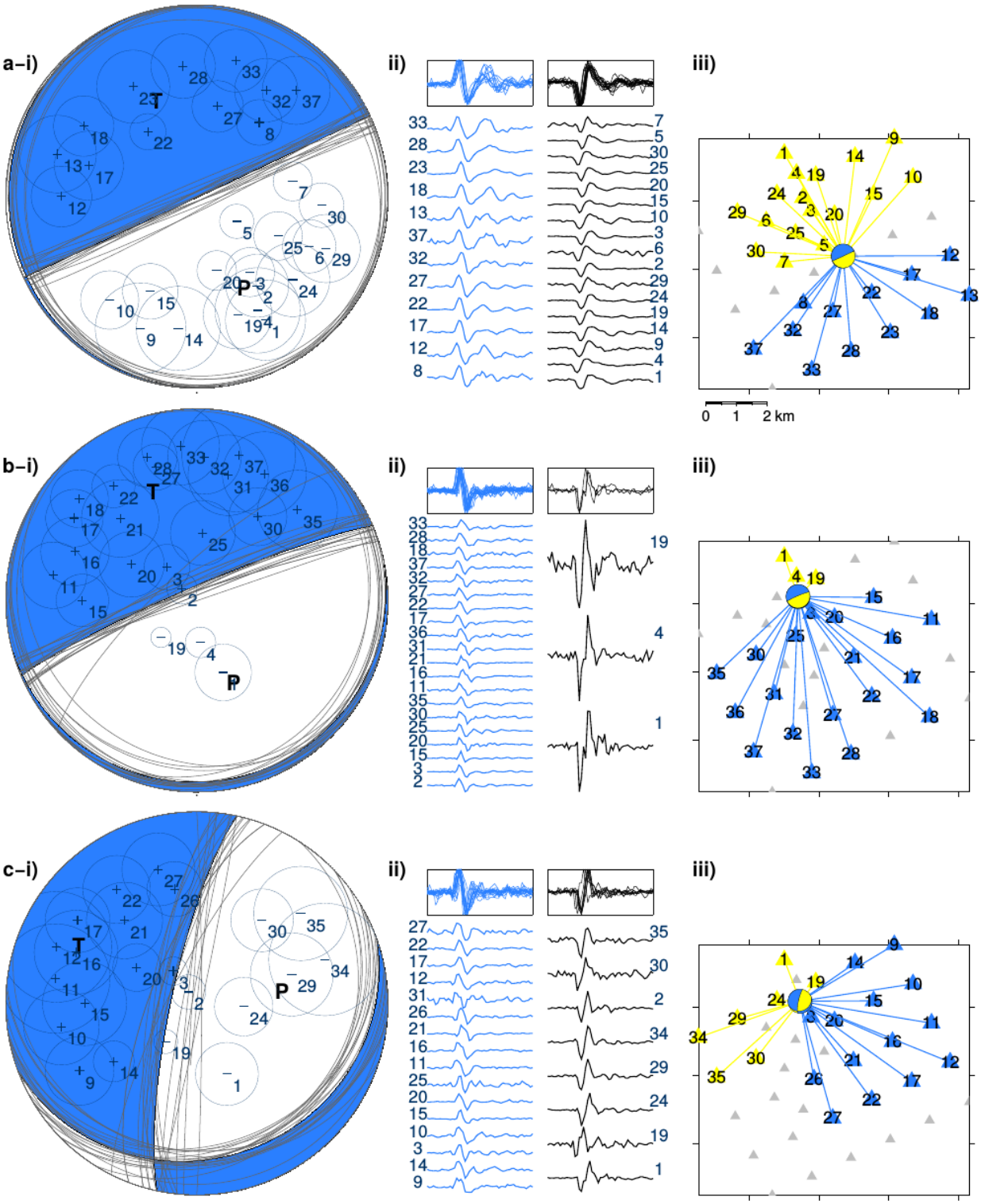

Figure 3: Example focal mechanisms. Subfigures a-c show three different sample events. Event a) is the same as in Figures 2a, S3 and S4. Events b (event time: 2019-01-03T04:36:40.244) and c

(event time: 2019-01-01T06:42:46.998) were chosen due to their location at the margin of the seismic network. i) Lower hemisphere projection of preferred mechanism (highlighted in blue). Gray nodal planes show other possible results from bootstrap analysis. Polarity picks (+/- signs) and amplitude ratios (normalised circles) are highlighted at the position of a specific station on the stereonet. Numbers refer to specific station indices as used in sub-figures i to iii to identify individual stations. ii) P-onsets (0.05 s time window; amplitudes normed) of all stations used to constrain the focal mechanisms. Colour coding indicates negative/positive onsets (blue – positive; black – negative). The top panel plots all results of one group on top of each other. iii) map view of the event location in the context of the network. Mechanism is shown in lower hemispheric projection. Colour coding of positive onsets as (ii); negative onsets are highlighted in yellow. Gray stations were not picked. All events locate at the ice-bed interface.

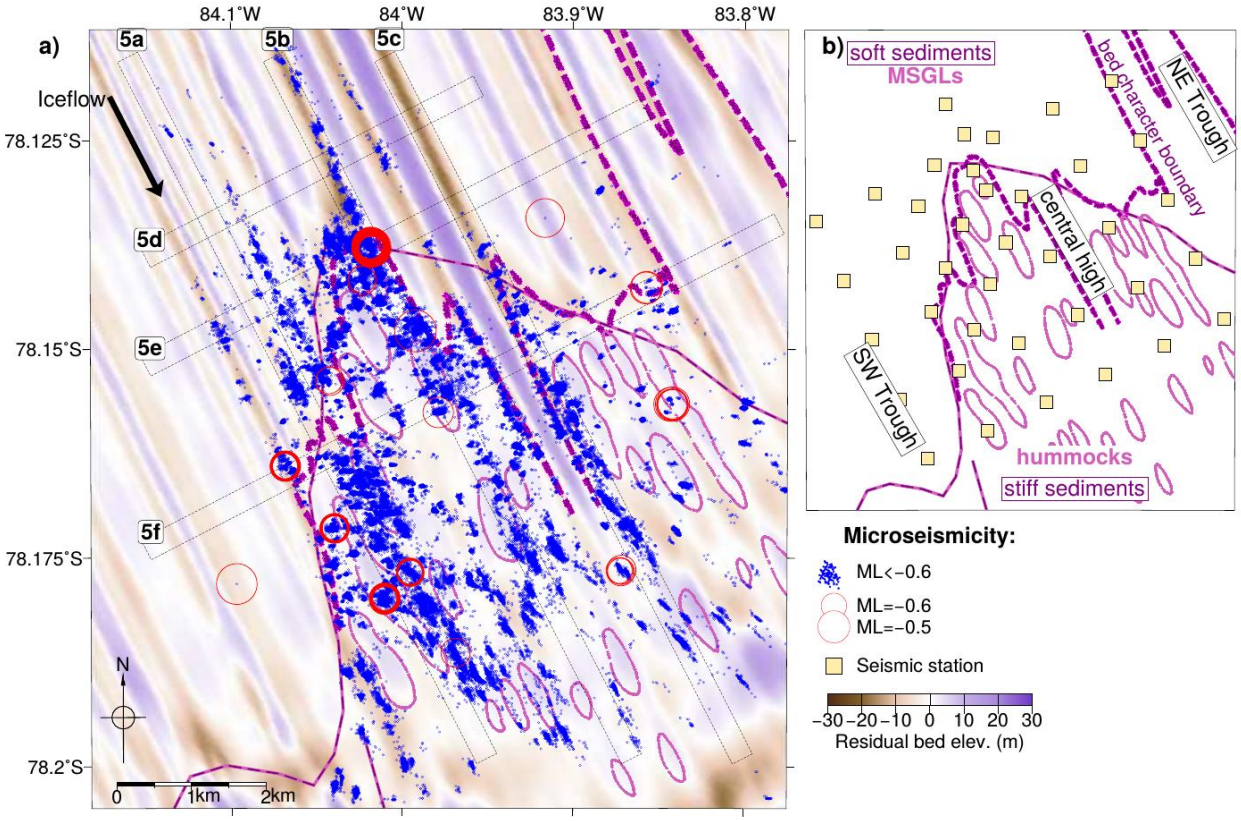

788

789 **Figure 4: Microseismic event catalogue.** a) Location of microseismicity in map view. Bed features
790 and geometry as in Figure 1c. See Figure S6 for further catalogue statistics. b) Simplified outline
791 of map domain to highlight geographic terms used in Sections 4-6. Seismic stations are plotted
792 as yellow rectangles.

793

794

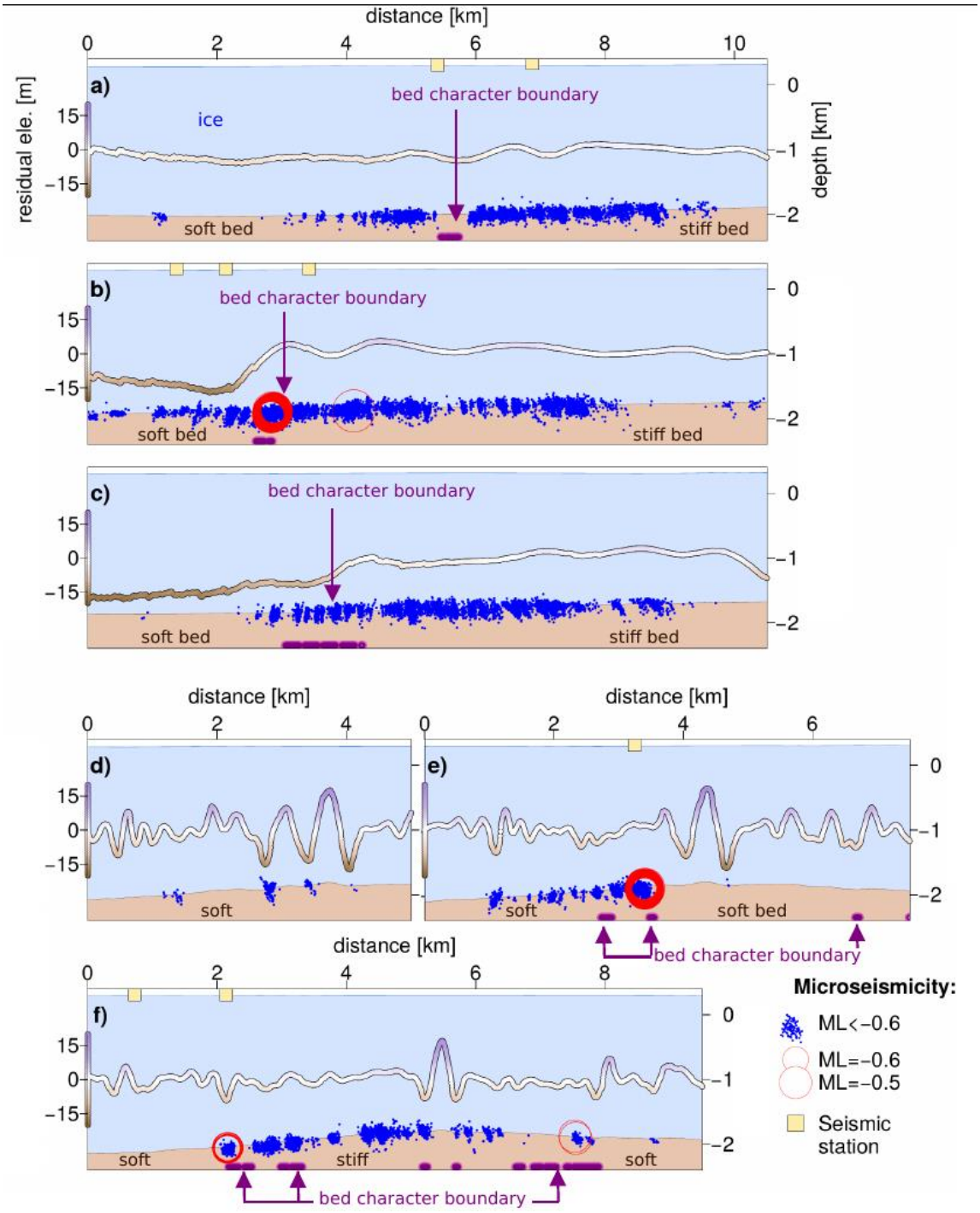

795

796 **Figure 5: Microseismic event catalogue in profile view.** a-c) Flow-parallel and d-f) flow-
797 perpendicular cross sections. Profile locations are highlighted in Fig. 4a). Residual topography is
798 projected onto the profiles for reference. Purple domains at the base of the profiles represent
799 intersection points of the profiles with the bed character boundary.

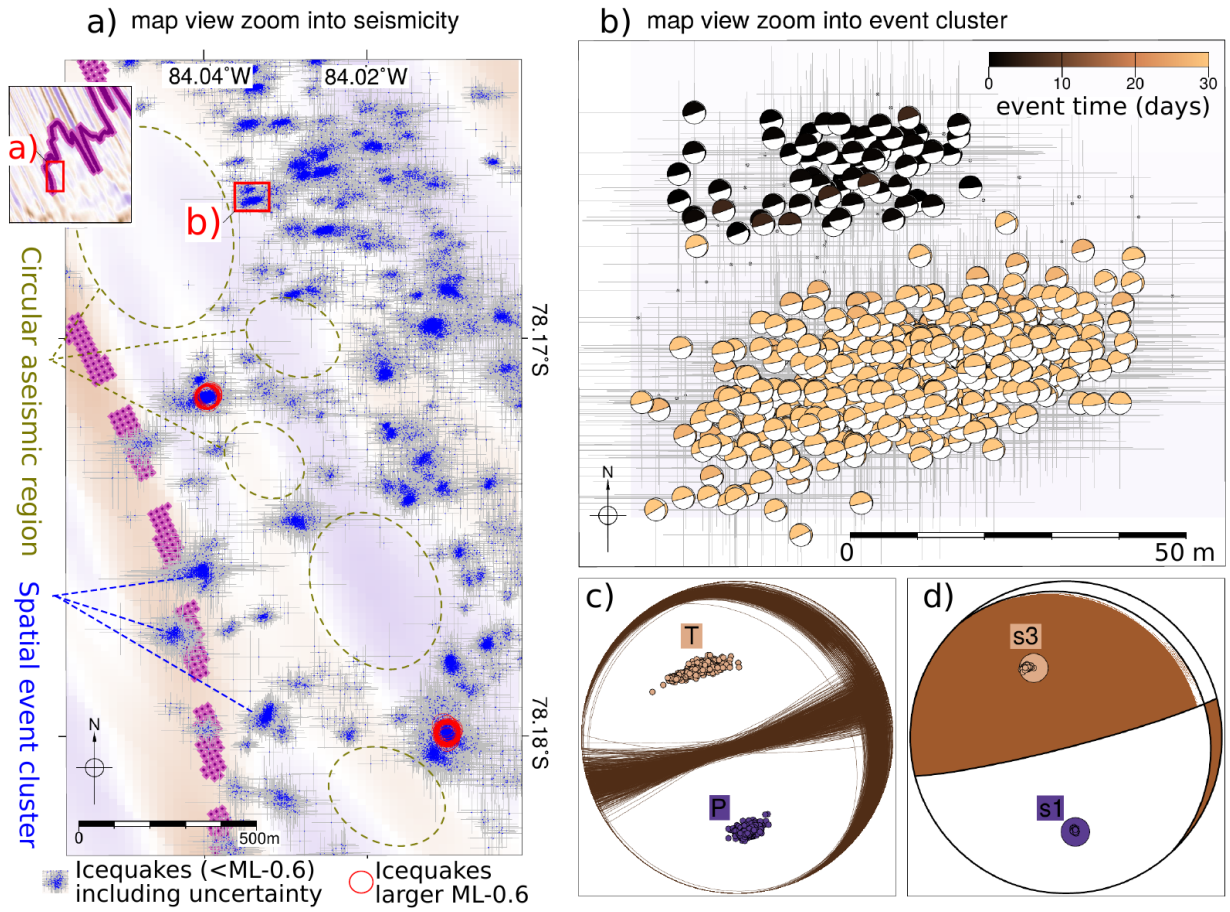

Figure 6: Zoom into a region of high microseismicity rate and stress inversion example. a) Microseismicity (blue) as in Figure 4a but plotted with horizontal location errors (grey). Large events (ML>-0.6) are highlighted in red. Bed character boundary and residual topography as in Figure 4a. Labels refer to features discussed in the text. Inset shows overview (same map extent as Figure 4a) highlighting the locations of a). b) Zoom into one event cluster (location of zoom shown as red box in a), showing the individual event focal mechanisms (lower hemisphere projection) at their geographic location in map view. Gray bars indicate horizontal location errors. Compressional quadrants are colour coded according to their event time relative to the first event in the cluster. c) Nodal plane of individual event mechanisms of this cluster with highlighted P/T axes plotted on top of each other. d) Resulting stress tensor of this cluster after inversion. Large brown/purple circles represent the sigma1/3 axes of the preferred stress tensor. Smaller circles are the results of bootstrap tests.

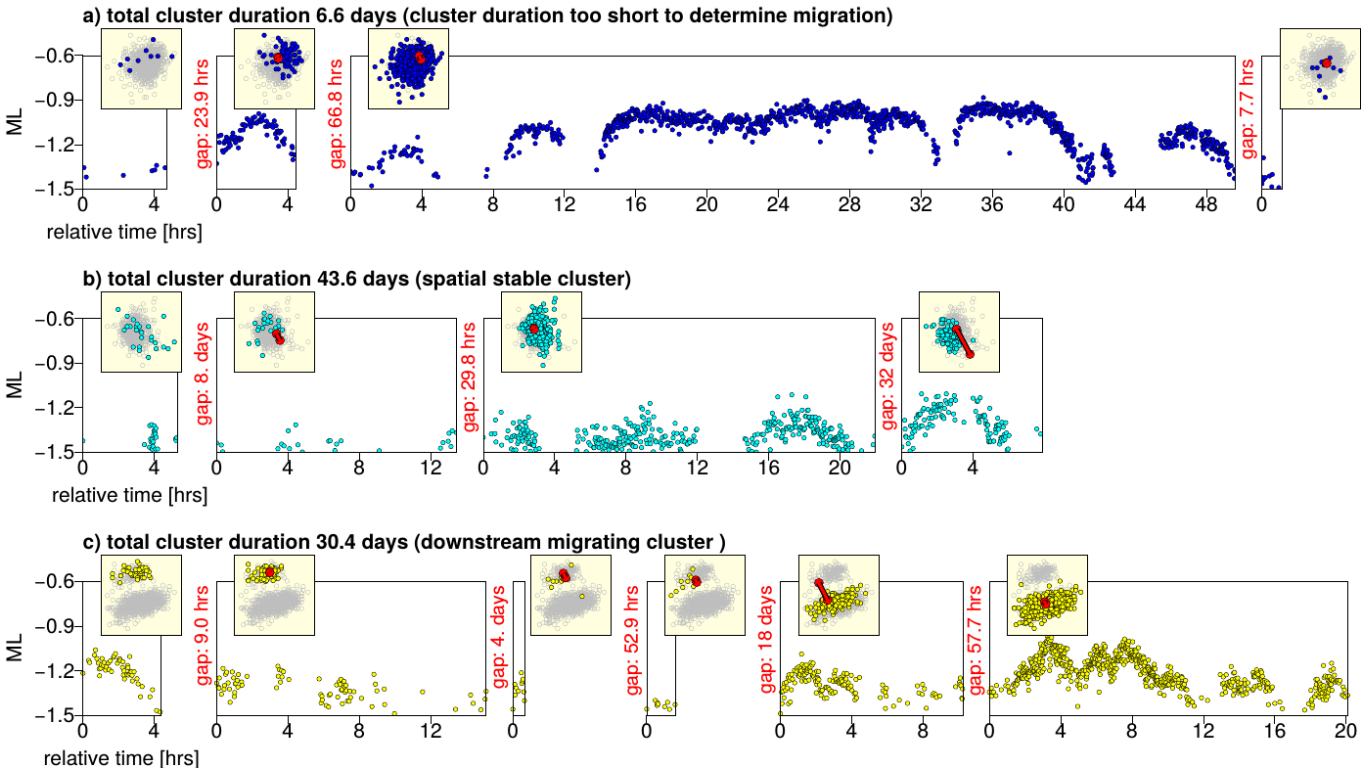

Figure 7: Zoom into spatiotemporal evolution of three example clusters. The main panels in a-c) show the evolution of event magnitude with time, the inset plots the event locations in map view. Note that the time axes are discontinuous: for inter-event times larger than five hours, the time axes are cut, and plotting is re-started when seismicity returns. The times of inactivity are given in red letters. In map view, events highlighted in same colour as graphs are active in a specific time step ('temporal sub-cluster'). Grey events are all events spatially attached to the specific cluster ('cluster'). Red circles and connection lines indicate the amount of downstream flow of RIS in the time a specific cluster has been inactive (assuming a flow rate of 1.05 $m\ day^{-1}$). The lines initiate at the sub-cluster centre of the previous sub-cluster activity. a) Example cluster for a short-lived cluster for which the time of total activity is too short to determine a trend in cluster migration. Cluster dimension in map view is 67x56 *m*. Starting time of the first sub-cluster is 2019-01-04T01:12. b) Example cluster in which cluster centroid does not appear to change with time, although significant downstream movement accumulates. Cluster dimension in map view is 104x92 *m*. Starting time of the first sub-cluster is 2018-12-20T04:48. c) Example cluster where the centroid changes with time in the same range as accumulated ice stream movement. Cluster

dimension in map view is 95x78 *m*. Starting time of the first sub-cluster is 2019-01-01T22:33. Cluster locations are highlighted in Figure 8b. A plot with location and magnitude errors included is attached in Figure S9.

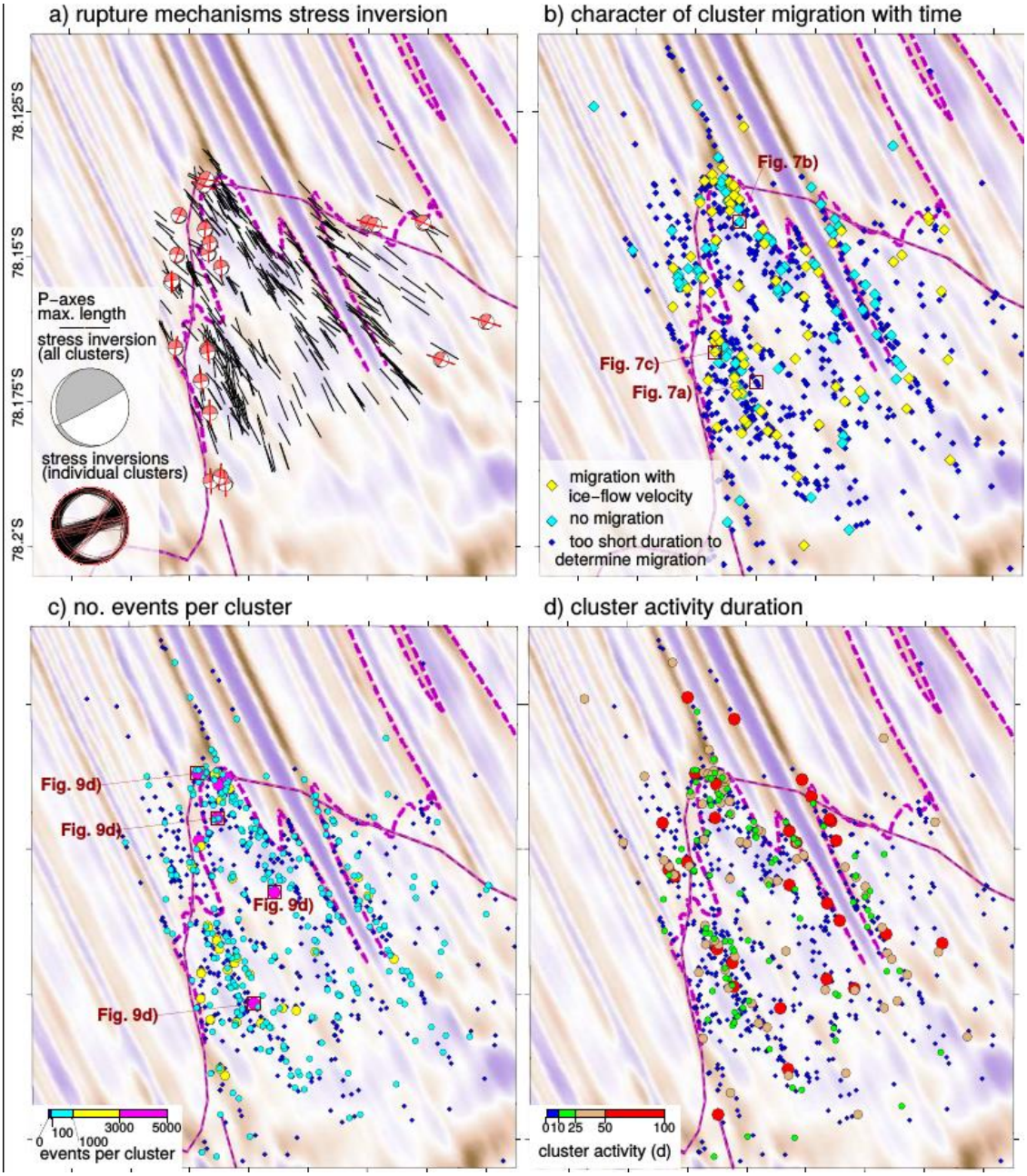

Figure 8: Event cluster characteristics. a) Stress inversion results from 70023 individual focal mechanisms, bundled into 428 clusters. For most inversion results only the P-axes, projected into map view, is shown. Only inversion results where P-axes azimuth deviates for more than 30° from the solution for all clusters are highlighted and plotted with mechanism. Inset: stress inversion for all clusters and nodal planes of individual inversions. Mechanism with large deviation are highlighted as in the map view. b) Clusters colour coded by character of cluster migration. Clusters shown in Figure 7 are highlighted. c) Cluster size split into small (blue; <100 events),

intermediate (turquoise; < 1000 events) and large (yellow/purple; up to 5000 events) clusters. d) Clusters colour coded according to their duration of activity. Activity duration is measured from the first to the last event occurring at a spatial spot. Within this time, the cluster may be active in several busts, separated by more quiet phases (‘temporal sub-clusters'), or continuously (see examples in Figs. 7, 9d).

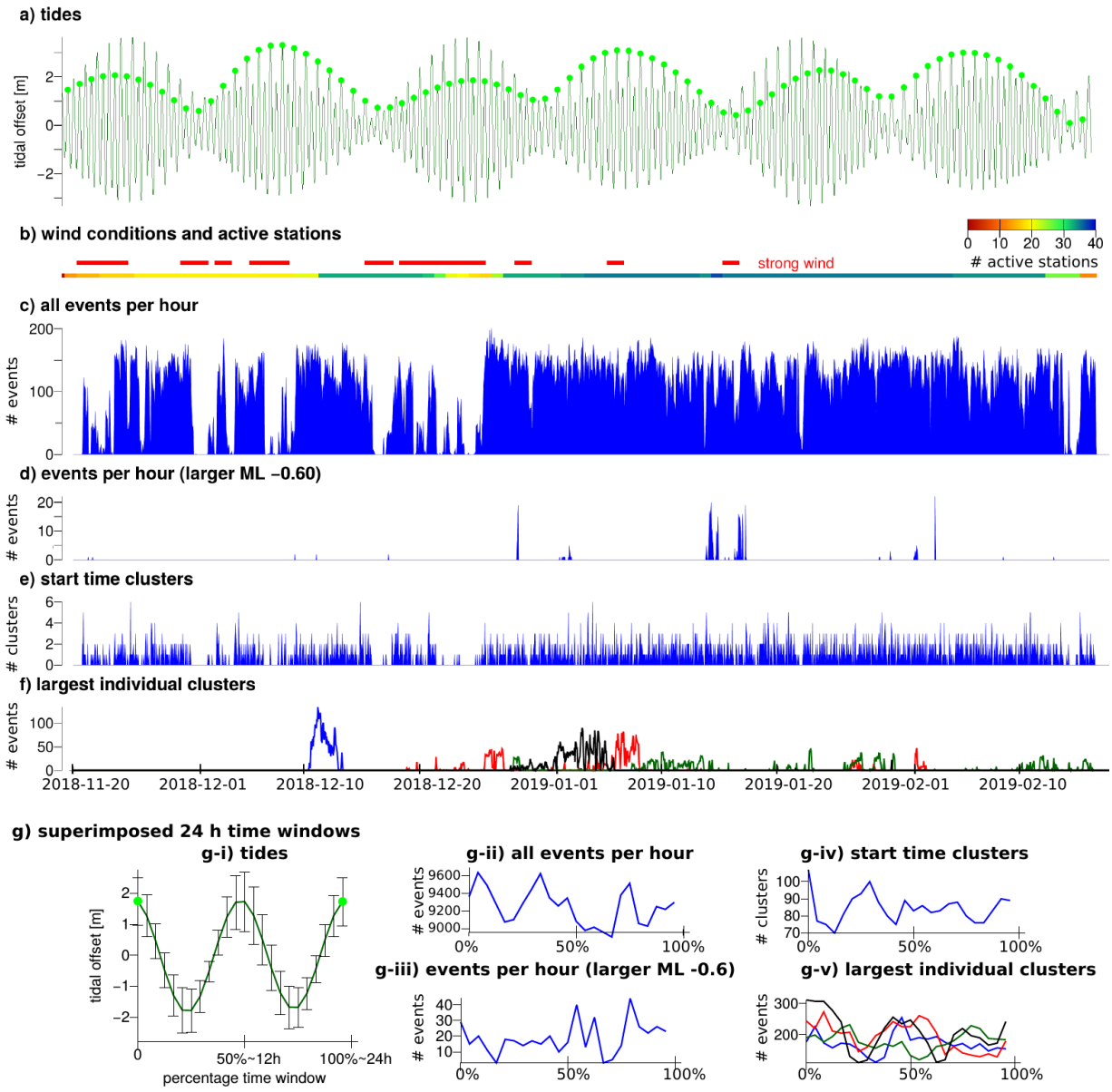

850

851 **Figure 9: Time series plots of event/cluster number and tidal modulations.** a) Tidal height at the
852 grounding line of RIS (82.8°W/78.6°S) calculated using the Padman tidal model code (Padman &
853 Erofeeva, 2004). The m2, s2, n2, k2, k1, o1, p1, q1, mf and mm mode are included in the model
854 calculation. Light green circles highlight the local tidal maximum of each ~24 h cycle. b) Wind
855 conditions and number of active stations. Periods of strong wind (according to field notes from
856 AB and AS) are marked with red bars. c) number of microseismic events with time. Events are
857 binned into one-hour sections. d) as c) but only events larger than ML=-0.6 are shown. e) as c)
858 but starting times of temporal sub-clusters are shown. f) as c) but the time evolution of four

859 individual clusters (plotted in different colours) is shown. Cluster locations are highlighted in
860 Figure 8c. g) Tidal cycles and event histograms collapsed into one tidal cycle (~24 h, two tidal
861 maxima as highlighted in a); Table S2 lists all time windows used to derive these plots).

862

863

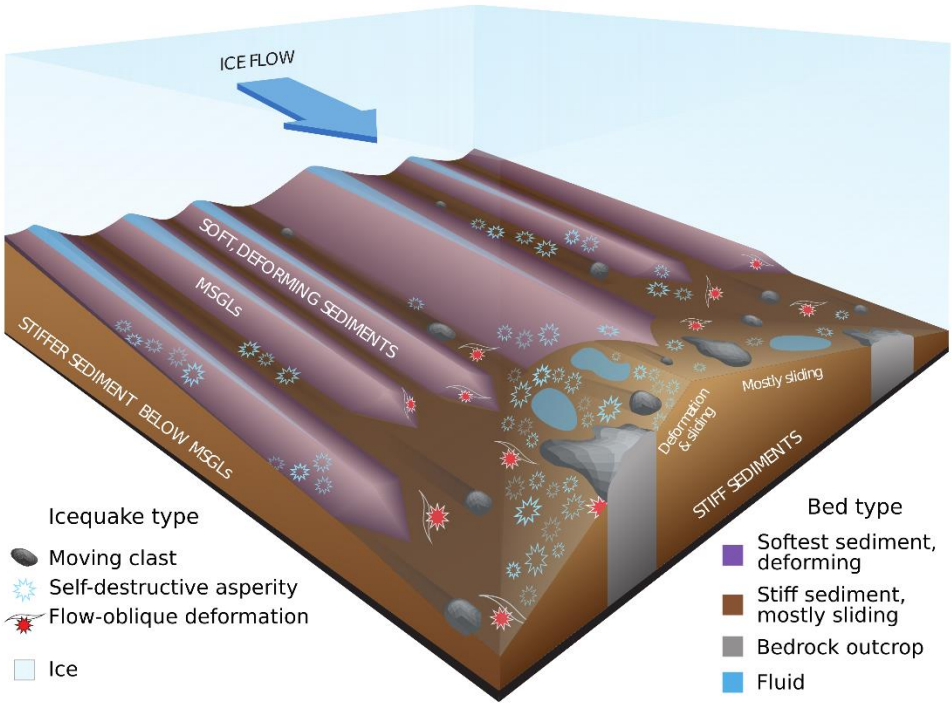

Figure 10: Schematic interpretation sketch on active basal processes. The loci of icequakes depend strongly on bed type, with most events occurring within the stiffer sediments. Different processes can trigger the icequakes. Among these, the continuous creation of sites of increased friction that develop due to sediment transport and/or due to temporal variable till properties within the bed (asperities) and their seismogenic destruction is most common.

References

Adalgeirsdóttir, G., Smith, A. M., Murray, T., King, M. A., Makinson, K., Nicholls, K. W., & Behar, A. E. (2008). Tidal influence on Rutford Ice Stream, West Antarctica: Observations of surface flow and basal processes from closely spaced GPS and passive seismic stations. *Journal of Glaciology*. https://doi.org/10.3189/002214308786570872

Anandakrishnan, S., & Alley, R. B. (1997). Tidal forcing of basal seismicity of ice stream C, West Antarctica, observed far inland. *Journal of Geophysical Research: Solid Earth*. https://doi.org/10.1029/97jb01073

Anandakrishnan, S., & Bentley, C. R. (1993). Micro-earthquakes beneath ice streams B and C, West Antarctica: observations and implications. *Journal of Glaciology*. https://doi.org/10.1017/s0022143000016348

Anandakrishnan, S., Voigt, D. E., Alley, R. B., & King, M. A. (2003). Ice stream D flow speed is strongly modulated by the tide beneath the Ross Ice Shelf. *Geophysical Research Letters*. https://doi.org/10.1029/2002GL016329

Anker, P. G. D., Makinson, K., Nicholls, K. W., & Smith, A. M. (2021). The BEAMISH hot water drill system and its use on the Rutford Ice Stream, Antarctica. *Annals of Glaciology*, 1–17. https://doi.org/10.1017/aog.2020.86

Barcheck, C. G., Schwartz, S. Y., & Tulaczyk, S. (2020). Icequake streaks linked to potential mega-scale glacial lineations beneath an Antarctic ice stream. *Geology*. https://doi.org/10.1130/G46626.1

Barcheck, C. G., Tulaczyk, S., Schwartz, S. Y., Walter, J. I., & Winberry, J. P. (2018). Implications of basal micro-earthquakes and tremor for ice stream mechanics: Stick-slip basal sliding and till erosion. *Earth and Planetary Science Letters*. https://doi.org/10.1016/j.epsl.2017.12.046

Benn, D., & Evens, D. J. A. (2014). *Glaciers and Glaciation, 2nd edition, Routledge*. https://doi.org/10.4324/9780203785010

Blankenship, D. D., Anandakrishnan, S., Kempf, J. L., & Bentley, C. R. (1987). Microearthquakes Under and Alongside Ice Stream B, Antarctica. Detected By A New Passive Seismic Array. *Annals of Glaciology*. https://doi.org/10.3189/s0260305500200712

Blankenship, D. D., Bentley, C. R., Rooney, S. T., & Alley, R. B. (1986). Seismic measurements reveal a saturated porous layer beneath an active Antarctic ice stream. *Nature*. https://doi.org/10.1038/322054a0

Bloch, W., Schurr, B., Kummerow, J., Salazar, P., & Shapiro, S. A. (2018). From Slab Coupling to Slab Pull: Stress Segmentation in the Subducting Nazca Plate. *Geophysical Research Letters*. https://doi.org/10.1029/2018GL078793

Boulton, G. S., & Hindmarsh, R. C. A. (1987). Sediment deformation beneath glaciers: rheology and geological consequences. *Journal of Geophysical Research*. https://doi.org/10.1029/JB092iB09p09059

Brune, J. N. (1970). Tectonic stress and the spectra of seismic shear waves from earthquakes. *J Geophys Res*. https://doi.org/10.1029/jb075i026p04997

Butcher, A., Luckett, R., Kendall, J. M., & Baptie, B. (2020). Seismic magnitudes, corner frequencies, and microseismicity: Using ambient noise to correct for high-frequency attenuation. *Bulletin of the Seismological Society of America*. https://doi.org/10.1785/0120190032

Danesi, S., Bannister, S., & Morelli, A. (2007). Repeating earthquakes from rupture of an asperity under an Antarctic outlet glacier. *Earth and Planetary Science Letters*. https://doi.org/10.1016/j.epsl.2006.10.023

Doake, C. S. M., Corr, H. F. J., Jenkins, A., Makinson, K., Nicholls, K. W., Nath, C., Smith, A. M., & Vaughan, D. G. (2013). *Rutford Ice Stream, Antarctica*. The West Antarctic Ice Sheet: Behavior and Environment, Antarct. Res. Ser., 77, 221-235. https://doi.org/10.1029/ar077p0221

El-Isa, Z. H., & Eaton, D. W. (2014). Spatiotemporal variations in the b-value of earthquake

magnitude-frequency distributions: Classification and causes. In *Tectonophysics*. https://doi.org/10.1016/j.tecto.2013.12.001

Feldmann, J., & Levermann, A. (2015). Collapse of the West Antarctic Ice Sheet after local destabilization of the Amundsen Basin. *Proceedings of the National Academy of Sciences of the United States of America*. https://doi.org/10.1073/pnas.1512482112

Fischer, T., Horálek, J., Hrubcová, P., Vavryčuk, V., Bräuer, K., & Kämpf, H. (2014). Intra-continental earthquake swarms in West-Bohemia and Vogtland: A review. In *Tectonophysics*. https://doi.org/10.1016/j.tecto.2013.11.001

Fischer, U. H., Clarke, G. K. C., & Blatter, H. (1999). Evidence for temporally varying "sticky spots" at the base of Trapridge Glacier, Yukon Territory, Canada. *Journal of Glaciology*. https://doi.org/10.3189/s0022143000001854

Fretwell, P., Pritchard, H. D., Vaughan, D. G., Bamber, J. L., Barrand, N. E., Bell, R., Bianchi, C., Bingham, R. G., Blankenship, D. D., Casassa, G., Catania, G., Callens, D., Conway, H., Cook, A. J., Corr, H. F. J., Damaske, D., Damm, V., Ferraccioli, F., Forsberg, R., … Zirizzotti, A. (2013). Bedmap2: Improved ice bed, surface and thickness datasets for Antarctica. *Cryosphere*. https://doi.org/10.5194/tc-7-375-2013

Greenfield, T., Keir, D., Kendall, J. M., & Ayele, A. (2019). Low-frequency earthquakes beneath Tullu Moye volcano, Ethiopia, reveal fluid pulses from shallow magma chamber. *Earth and Planetary Science Letters*. https://doi.org/10.1016/j.epsl.2019.115782

Gudmundsson, G. H. (2006). Fortnightly variations in the flow velocity of Rutford Ice Stream, West Antarctica. *Nature*. https://doi.org/10.1038/nature05430

Gutenberg, B., & Richter, C. F. (1944). Frequency of earthquakes in California. *Bull. Seism. Soc. Am.*, *34*, 185–188.

Hanks, T. C., & Kanamori, H. (1979). A moment magnitude scale. *Journal of Geophysical Research B: Solid Earth*. https://doi.org/10.1029/JB084iB05p02348

Hardebeck, J. L., & Shearer, P. M. (2002). A new method for determining first-motion focal

mechanisms. *Bulletin of the Seismological Society of America*. https://doi.org/10.1785/0120010200

Hardebeck, J. L., & Shearer, P. M. (2003). Using S/P amplitude ratios to constrain the focal mechanisms of small earthquakes. *Bulletin of the Seismological Society of America*. https://doi.org/10.1785/0120020236

Helmstetter, A., Lipovsky, B. P., Larose, E., Baillet, L., & Mayoraz, R. (2018). Repeating quakes triggered by snow-falls at Gugla rock-glacier: transition between stable slip and stickslip. *Annual Meeting of the Seismological Society of America, Seims. Res. Lett*, *89*(2B).

Helmstetter, A., Nicolas, B., Comon, P., & Gay, M. (2015). Basal icequakes recorded beneath an alpine glacier (Glacier d'Argentière, Mont Blanc, France): Evidence for stick-slip motion? *Journal of Geophysical Research: Earth Surface*. https://doi.org/10.1002/2014JF003288

Hudson, T. S., Brisbourne, A. M., Walter, F., Gräff, D., White, R. S., & Smith, A. M. (2020). Icequake source mechanisms for studying glacial sliding. *Journal of Geophysical Research: Earth Surface*, *125(11)*. https://doi.org/e2020JF005627

Hudson, T. S., Smith, J., Brisbourne, A. M., & White, R. S. (2019). Automated detection of basal icequakes and discrimination from surface crevassing. *Annals of Glaciology*. https://doi.org/10.1017/aog.2019.18

Iverson, N. R. (2011). Shear resistance and continuity of subglacial till: Hydrology rules. In *Journal of Glaciology*. https://doi.org/10.3189/002214311796406220

Kettlety, T., Verdon, J. P., Werner, M. J., Kendall, J. M., & Budge, J. (2019). Investigating the role of elastostatic stress transfer during hydraulic fracturing-induced fault activation. *Geophysical Journal International*. https://doi.org/10.1093/gji/ggz080

King, E. C., Hindmarsh, R. C. A., & Stokes, C. R. (2009). Formation of mega-scale glacial lineations observed beneath a West Antarctic ice stream. *Nature Geoscience*. https://doi.org/10.1038/ngeo581

King, E. C., Pritchard, H. D., & Smith, A. M. (2016). Subglacial landforms beneath Rutford Ice

975 Stream, Antarctica: detailed bed topography from ice-penetrating radar. *Earth System*
976 *Science Data*. https://doi.org/10.5194/essd-8-151-2016

977 King, E. C., Woodward, J., & Smith, A. M. (2004). Seismic evidence for a water-filled canal in
978 deforming till beneath Rutford Ice Stream, West Antarctica. *Geophysical Research Letters*.
979 https://doi.org/10.1029/2004GL020379

980 Kufner, S.-K., Brisbourne, A., Smith, A., Hudson, T., Murray, T., Schlegel, R., Kendall, J.,
981 Anandakrishnan, S., & Lee, I. (2020). Microseismic icequake catalogue, Rutford Ice Stream
982 (West Antarctica), November 2018 to February 2019 (Version 1.0) [Data set]. *UK Polar*
983 *Data Centre, Natural Environment Research Council, UK Research & Innovation*.
984 https://doi.org/10.5285/B809A040-8305-4BC5-BAFF-76AA2B823734

985 Lee, William Hung Kan, & Lahr, J. C. (1972). HYPO71: A computer program for determining
986 hypocenter, magnitude, and first motion pattern of local earthquakes. *US Department of*
987 *the Interior, Geological Survey, National Center for Earthquake Research*.

988 Lipovsky, B. P., Meyer, C. R., Zoet, L. K., McCarthy, C., Hansen, D. D., Rempel, A. W., & Gimbert,
989 F. (2019). Glacier sliding, seismicity and sediment entrainment. *Annals of Glaciology*.
990 https://doi.org/10.1017/aog.2019.24

991 Lomax, A., Virieux, J., Volant, P., & Berge-Thierry, C. (2000). *Probabilistic Earthquake Location in*
992 *3D and Layered Models*. https://doi.org/10.1007/978-94-015-9536-0_5

993 Maurel, A., Lund, F., & Montagnat, M. (2015). Propagation of elastic waves through textured
994 polycrystals: Application to ice. *Proceedings of the Royal Society A: Mathematical, Physical*
995 *and Engineering Sciences*. https://doi.org/10.1098/rspa.2014.0988

996 McBrearty, I. W., Zoet, L. K., & Anandakrishnan, S. (2020). Basal seismicity of the Northeast
997 Greenland Ice Stream. *Journal of Glaciology*. https://doi.org/10.1017/jog.2020.17

998 Michael, A. J. (1987). Use of focal mechanisms to determine stress: a control study. *Journal of*
999 *Geophysical Research*. https://doi.org/10.1029/JB092iB01p00357

1000 Minchew, B. M., Simons, M., Riel, B., & Milillo, P. (2017). Tidally induced variations in vertical

and horizontal motion on Rutford Ice Stream, West Antarctica, inferred from remotely sensed observations. *Journal of Geophysical Research: Earth Surface*. https://doi.org/10.1002/2016JF003971

Murray, T., Corr, H., Forieri, A., & Smith, A. M. (2008). Contrasts in hydrology between regions of basal deformation and sliding beneath Rutford Ice Stream, West Antarctica, mapped using radar and seismic data. *Geophysical Research Letters*. https://doi.org/10.1029/2008GL033681

Murray, T., Smith, A. M., King, M. A., & Weedon, G. P. (2007). Ice flow modulated by tides at up to annual periods at Rutford Ice Stream, West Antarctica. *Geophysical Research Letters*. https://doi.org/10.1029/2007GL031207

Padman, L., & Erofeeva, S. (2004). A barotropic inverse tidal model for the Arctic Ocean. *Geophysical Research Letters*. https://doi.org/10.1029/2003GL019003

Pedregosa, F., Varoquaux, G., Gramfort, A., Michel, V., Thirion, B., Grisel, O., Blondel, M., Prettenhofer, P., Weiss, R., Dubourg, V., Vanderplas, J., Passos, A., Cournapeau, D., Brucher, M., Perrot, M., & Duchesnay, É. (2011). Scikit-learn: Machine learning in Python. *Journal of Machine Learning Research*, *12*, 2825–2830.

Piotrowski, J. A., Larsen, N. K., & Junge, F. W. (2004). Reflections on soft subglacial beds as a mosaic of deforming and stable spots. *Quaternary Science Reviews*. https://doi.org/10.1016/j.quascirev.2004.01.006

Pratt, M. J., Winberry, J. P., Wiens, D. A., Anandakrishnan, S., & Alley, R. B. (2014). Seismic and geodetic evidence for grounding-line control of Whillans Ice Stream stick-slip events. *Journal of Geophysical Research: Earth Surface*. https://doi.org/10.1002/2013JF002842

Rathbun, A. P., Marone, C., Alley, R. B., & Anandakrishnan, S. (2008). Laboratory study of the frictional rheology of sheared till. *Journal of Geophysical Research: Earth Surface*. https://doi.org/10.1029/2007JF000815

Reinardy, B. T. I., Larter, R. D., Hillenbrand, C. D., Murray, T., Hiemstra, J. F., & Booth, A. D.

(2011). Streaming flow of an Antarctic Peninsula palaeo-ice stream, both by basal sliding and deformation of substrate. *Journal of Glaciology*. https://doi.org/10.3189/002214311797409758

Richter, C. (1935). An instrumental earthquake magnitude scale. *Bulletin of the Seismological Society of America*, *25*(1), 1–32.

Rignot, E., Mouginot, J., & Scheuchl, B. (2011). Ice flow of the antarctic ice sheet. *Science*. https://doi.org/10.1126/science.1208336

Ritz, C., Edwards, T. L., Durand, G., Payne, A. J., Peyaud, V., & Hindmarsh, R. C. A. (2015). Potential sea-level rise from Antarctic ice-sheet instability constrained by observations. *Nature*. https://doi.org/10.1038/nature16147

Robel, A. A., Seroussi, H., & Roe, G. H. (2019). Marine ice sheet instability amplifies and skews uncertainty in projections of future sea-level rise. *Proceedings of the National Academy of Sciences of the United States of America*. https://doi.org/10.1073/pnas.1904822116

Robert W Jacobel, Brian C Welch, David Osterhouse, Rickard Pettersson, & Joseph A Macgregor. (2009). Spatial variation of radar-derived basal conditions on Kamb Ice Stream, West Antarctica. *Annals of Glaciology*. https://doi.org/10.3189/172756409789097504

Röösli, C., Helmstetter, A., Walter, F., & Kissling, E. (2016). Meltwater influences on deep stick-slip icequakes near the base of the Greenland Ice Sheet. *Journal of Geophysical Research: Earth Surface*. https://doi.org/10.1002/2015JF003601

Rosier, S. H. R., Gudmundsson, G. H., & Green, J. A. M. (2015). Temporal variations in the flow of a large Antarctic ice stream controlled by tidally induced changes in the subglacial water system. *Cryosphere*. https://doi.org/10.5194/tc-9-1649-2015

Schlaphorst, D., Kendall, J. M., Baptie, B., Latchman, J. L., & Tait, S. (2017). Gaps, tears and seismic anisotropy around the subducting slabs of the Antilles. *Tectonophysics*. https://doi.org/10.1016/j.tecto.2017.01.002

Schlegel, R., Murray, T., Smith, A. M., Brisbourne, A. M., Booth, A. D., King, E. C., & Clark, R. A.

(2021). Spatial Variation in Radar-Derived Basal Properties of Rutford Ice Stream, West Antarctica. *Earth and Space Science Open Archive*. https://doi.org/10.1002/essoar.10505715.1

Shearer, P. M. (2009). *Introduction to Seismology, Cambridge University Press*. https://doi.org/10.1017/cbo9780511841552

Smith, A. M. (1997). Basal conditions on Rutford Ice Stream, West Antarctica, from seismic observations. *Journal of Geophysical Research B: Solid Earth*. https://doi.org/10.1029/96jb02933

Smith, A. M. (2006). Microearthquakes and subglacial conditions. *Geophysical Research Letters*. https://doi.org/10.1029/2006GL028207

Smith, A. M., Anker, P. G. D., Nicholls, K. W., Makinson, K., Murray, T., Costas-Rios, S., Brisbourne, A. M., Hodgson, D. A., Schlegel, R., & Anandkrishnan, S. (2020). Ice stream subglacial access for ice sheet history and fast ice flow: The BEAMISH Project on Rutford Ice Stream, West Antarctica and initial results on basal conditions. *Annals of Glaciology*, 1–9. https://doi.org/10.1017/aog.2020.82

Smith, A. M., & Murray, T. (2009). Bedform topography and basal conditions beneath a fast-flowing West Antarctic ice stream. *Quaternary Science Reviews*. https://doi.org/10.1016/j.quascirev.2008.05.010

Smith, A. M., Murray, T., Nicholls, K. W., Makinson, K., Adalgeirsdóttir, G., Behar, A. E., & Vaughan, D. G. (2007). Rapid erosion, drumlin formation, and changing hydrology beneath an Antarctic ice stream. *Geology*. https://doi.org/10.1130/G23036A.1

Smith, E. C., Baird, A. F., Kendall, J. M., Martín, C., White, R. S., Brisbourne, A. M., & Smith, A. M. (2017). Ice fabric in an Antarctic ice stream interpreted from seismic anisotropy. *Geophysical Research Letters*. https://doi.org/10.1002/2016GL072093

Smith, E. C., Smith, A. M., White, R. S., Brisbourne, A. M., & Pritchard, H. D. (2015). Mapping the ice-bed interface characteristics of Rutford Ice Stream, West Antarctica, using

microseismicity. *Journal of Geophysical Research F: Earth Surface*. https://doi.org/10.1002/2015JF003587

Smith, J. D., White, R. S., Avouac, J.-P., & Bourne, S. (2020). Probabilistic earthquake locations of induced seismicity in the Groningen region, the Netherlands. *Geophysical Journal International*. https://doi.org/10.1093/gji/ggaa179

Stokes, C. R. (2018). Geomorphology under ice streams: Moving from form to process. In *Earth Surface Processes and Landforms*. https://doi.org/10.1002/esp.4259

Thomason, J. F., & Iverson, N. R. (2008). A laboratory study of particle ploughing and pore-pressure feedback: A velocity-weakening mechanism for soft glacier beds. *Journal of Glaciology*. https://doi.org/10.3189/002214308784409008

Thornsteinsson, T., & Raymond, C. F. (2000). Sliding versus till deformation in the fast motion of an ice stream over a viscous till. *Journal of Glaciology*. https://doi.org/10.3189/172756500781832729

Tsai, V. C., Stewart, A. L., & Thompson, A. F. (2015). Marine ice-sheet profiles and stability under Coulomb basal conditions. *Journal of Glaciology*. https://doi.org/10.3189/2015JoG14J221

USGS. (2007). *Landsat Image Mosaic of Antarctica (LIMA) U.S Geological Survey Fact Sheet 2007–3116, 4 p.*

Van Der Meer, J. J. M., Menzies, J., & Rose, J. (2003). Subglacial till: The deforming glacier bed. *Quaternary Science Reviews*. https://doi.org/10.1016/S0277-3791(03)00141-0

Vankova, I., & Nicholls, K. W. (2019). Using ApRES to infer tidal melt rates and vertical strain rates at the Filchner-Ronne Ice Shelf. *Geophysical Research Abstracts*, Vol. 21.

Walter, F., Canassy, P. D., Husen, S., & Clinton, J. F. (2013). Deep icequakes: What happens at the base of alpine glaciers? *Journal of Geophysical Research: Earth Surface*. https://doi.org/10.1002/jgrf.20124

Walter, F., Deichmann, N., & Funk, M. (2008). Basal icequakes during changing subglacial water

pressures beneath Gornergletscher, Switzerland. *Journal of Glaciology*. https://doi.org/10.3189/002214308785837110

Wilks, M., Kendall, J. M., Nowacki, A., Biggs, J., Wookey, J., Birhanu, Y., Ayele, A., & Bedada, T. (2017). Seismicity associated with magmatism, faulting and hydrothermal circulation at Aluto Volcano, Main Ethiopian Rift. *Journal of Volcanology and Geothermal Research*. https://doi.org/10.1016/j.jvolgeores.2017.04.003

Winberry, J. P., Anandakrishnan, S., Wiens, D. A., & Alley, R. B. (2013). Nucleation and seismic tremor associated with the glacial earthquakes of Whillans Ice Stream, Antarctica. *Geophysical Research Letters*. https://doi.org/10.1002/grl.50130

Zoet, L. K., & Iverson, N. R. (2020). A slip law for glaciers on deformable beds. *Science*. https://doi.org/10.1126/science.aaz1183